

Manuscript Number:

Title: Effect of scCO<sub>2</sub>-brine mixture on injectivity and storage capacity  
in naturally fractured carbonate formations

Article Type: Full Length Article

Keywords: Fines migration; Effective porosity; Fractured acidizing;  
Formation permeability; Carbonate dissolution

Corresponding Author: Dr. Laura M Valle, Ph.D.

Corresponding Author's Institution: Escuela Técnica Superior de  
Ingenieros de Mina y Energía

First Author: Laura M Valle, Ph.D.

Order of Authors: Laura M Valle, Ph.D.; Carlos Grima, PhD; Ramón  
Rodríguez, Ph.D.; Carlos Llopis, Ph.D.

Abstract: The presence of natural fractures in the formation and its degree of heterogeneity condition the injection of CO<sub>2</sub> into the aquifer as they affect the migration processes and its storage capacity. In ATAP experimental facility the petrophysical behavior of two carbonate formations was studied, with different proportions of limestone, dolomite, quartz and anhydrite and fissures sealed mainly by potassium aluminosilicates and iron sulphides. Actual storage conditions (135/141 bar and 44/46 °C) corresponding to a depth of around 1500 m and continuous injection at a constant flow rate of 1cc/min of 10% and 15% of HCl, HCl/Acetic (CH<sub>3</sub>COOH) 10%/10% and scCO<sub>2</sub> (supercritical CO<sub>2</sub>)/brine 50%/50%, was applied to the brine saturated rock samples (coreflooding). Considering laminar flow through the fractures, the flow injected is proportional to the pressure drop according to the "cubic law" that takes into account the width and length of the fractures. This is used to evaluate the injectivity of the storage. The variations in the pressure drop are due to the dragging of detached fines in the dissolution of the carbonates of the filled fissures that can cause their opening or blocking. The efficacy of pure scCO<sub>2</sub> enriched brine injection was determined to dissolve the carbonates of the store formation compared to other methods such as the injection of acids used in the oil industry for the stimulation of producing wells. Scanning Electron Microscope (SEM) studies of the injection surfaces and Computerized Tomography (CT) analysis of the samples before and after injection of the acid mixtures have been performed. The dissolution facilitates the injectivity and increases the capacity favoring the tightness of the storage by the phenomenon of controlled dissolution-precipitation of the carbonates.

Research Data Related to this Submission

-----  
There are no linked research data sets for this submission. The following reason is given:

Data will be made available on request



## Journal of Natural Gas Science and Engineering

### Effect of scCO<sub>2</sub>-brine mixture on the injectivity and storage capacity in naturally fractured carbonate formations

L. M. Valle,<sup>1</sup> C. Grima,<sup>1</sup> R. Rodríguez,<sup>1</sup> C. Llopis,<sup>2</sup>

<sup>1</sup>Polytechnic University of Madrid

<sup>2</sup>Polytechnic University of Valencia

To Associate Editor or Executive Editor:

From a thorough appraisal of the existing publications it is recommended to improve the research in entire processes involved in the CO<sub>2</sub> sequestration operations and in situ mechanisms.

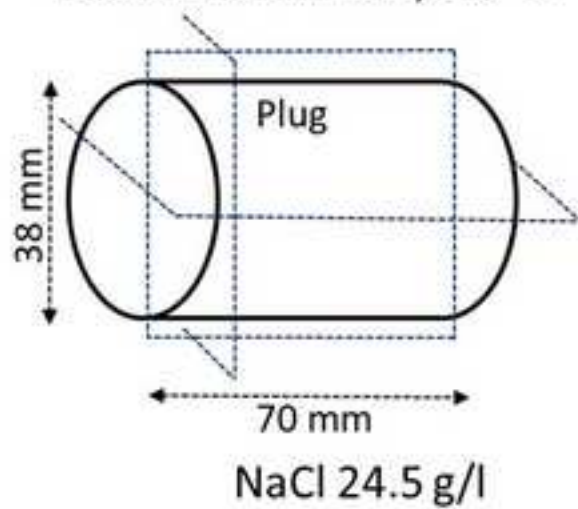
The patent *ATAP (P201231913.2015)* allows through its different configurations to study the injectivity and different trap mechanisms present in the aquifer.

Experiences on CO<sub>2</sub> injections in carbonates aquifers for permanent trapping are quite limited. The behavior of fractures in carbonates plays a key role in those reservoirs in which porous matrix permeability is very poor, which drives the CO<sub>2</sub> plume migration through the fracture network where hydromechanics and geochemical effects take place due to injection.

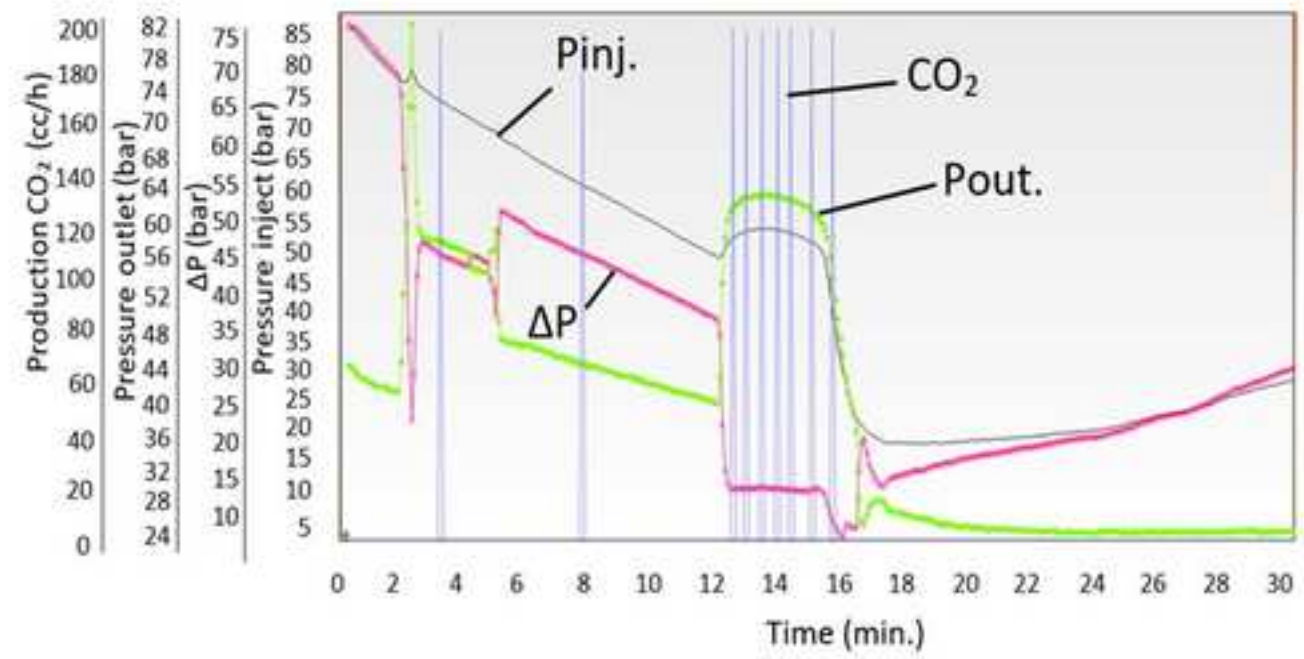
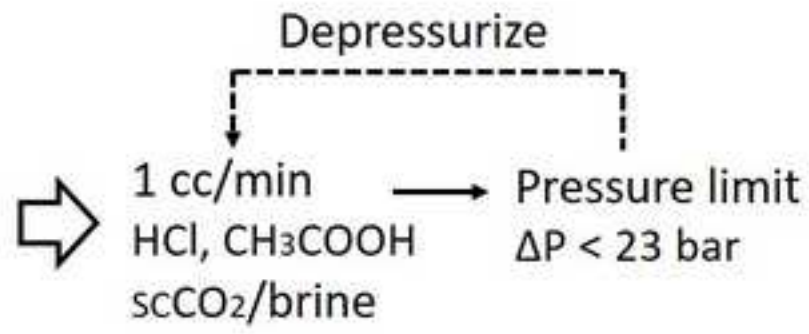
This paper compares the efficacy of pure scCO<sub>2</sub> enriched brine injection to dissolve the carbonates of the store formation surrounding the fissures for increasing the effective porosity of storage to other methods such as the injection of acids used in the oil industry for the stimulation of producing wells.

The increase of effective porosity using pure scCO<sub>2</sub> enriched brine injection facilitates the injectivity and increases the capacity favoring the tightness of the storage by the phenomenon of controlled dissolution-precipitation of the carbonates through the trap mechanisms of solubility trapping and mineral trapping. The use of scCO<sub>2</sub> enriched brine against the injection of acids to improve the injectivity, supposes a safe operation of storage, presenting itself as an economically and technically profitable alternative for the susceptible aquifers to store CO<sub>2</sub>.

Limestone 135 bar; 44° C  
Dolomite 141 bar; 46° C



INJECTION



### Highlights

1. Study of two naturally fractured carbonates formations for CO<sub>2</sub> storage in ATAP experimental facility using “cubic law” through fractures.
2. Core-flooding of HCl, HCl/Acetic and scCO<sub>2</sub>/brine in brine saturated storage rock at storage conditions.
3. Injection of scCO<sub>2</sub> enriched brine to increase the effective porosity of storage against the use of HCl, Acetic.
4. Study of the injection process efficacy in the increase of storage injectivity and capacity through SEM, CT.

# Effect of scCO<sub>2</sub>-brine mixture on injectivity and storage capacity in naturally fractured carbonate formations

L. M. Valle,<sup>1</sup> C. Grima,<sup>1</sup> R. Rodríguez,<sup>1</sup> C. Llopis,<sup>2</sup>

<sup>1</sup> Polytechnic University of Madrid

<sup>2</sup> Polytechnic University of Valencia

## ABSTRACT

The presence of natural fractures in the formation and its degree of heterogeneity condition the injection of CO<sub>2</sub> into the aquifer as they affect the migration processes and its storage capacity. In ATAP experimental facility the petrophysical behavior of two carbonate formations was studied, with different proportions of limestone, dolomite, quartz and anhydrite and fissures sealed mainly by potassium aluminosilicates and iron sulphides. Actual storage conditions (135/141 bar and 44/46 °C) corresponding to a depth of around 1500 m and continuous injection at a constant flow rate of 1cc/min of 10% and 15% of HCl, HCl/Acetic (CH<sub>3</sub>COOH) 10%/10% and scCO<sub>2</sub> (supercritical CO<sub>2</sub>)/brine 50%/50%, was applied to the brine saturated rock samples (coreflooding). Considering laminar flow through the fractures, the flow injected is proportional to the pressure drop according to the "cubic law" that takes into account the width and length of the fractures. This is used to evaluate the injectivity of the storage. The variations in the pressure drop are due to the dragging of detached fines in the dissolution of the carbonates of the filled fissures that can cause their opening or blocking. The efficacy of pure scCO<sub>2</sub> enriched brine injection was determined to dissolve the carbonates of the store formation compared to other methods such as the injection of acids used in the oil industry for the stimulation of producing wells. Scanning Electron Microscope (SEM) studies of the injection surfaces and Computerized Tomography (CT) analysis of the samples before and after injection of the acid mixtures have been performed. The dissolution facilitates the injectivity and increases the capacity favoring the tightness of the storage by the phenomenon of controlled dissolution-precipitation of the carbonates.

<i>Nomenclature</i>		T	Temperature
A	Cross sectional area	v	Apparent velocity
a <sub>i</sub>	Coefficients of K approximation	W <sub>s</sub>	Sample weight
F	Frontal	X	Longitudinal
f <sub>a</sub>	Fracture aperture	Y	Axial
F <sub>d</sub>	Geological formation		
h	Thickness of reservoir		
l	Fracture trace length	<i>Greek symbols</i>	
l <sub>0</sub>	Length of the structural unit	ΔP	Incremental pressure
K	Permeability	μ	Brine/fluid viscosity
L	Length of the plug	∅	Porosity
P	Pressure	ΔP <sub>f</sub>	Pres. drop across fracture along flow direction
P <sub>p1</sub>	Pore pressure far from the well		
P <sub>p2</sub>	Pore pressure near the well	<i>Abbreviations</i>	
q	Flow rate	ATAP	High Temperature High Pressure
R	Radial distance	BPR	Back pressure
r <sub>1</sub>	Reservoir radius	CT	Computerized Tomography
r <sub>2</sub>	Well Radius	scCO <sub>2</sub>	Supercritical CO <sub>2</sub>
SC	Sopeña Calizo	SEM	Scanning Electron Microscope
SD	Sopeña Dolomítico	XRD	X-Ray diffraction

## 32 1. Introduction

33 Injectivity and capacity are two of the most important parameters that influence the technical-  
 34 economic viability and safety of deep CO<sub>2</sub> storage (Hurtado, A., 2012). The development of the  
 35 CO<sub>2</sub> sequestration process requires maintaining sustained injectivity that turns out to be little  
 36 or null in the absence of effective porosity that is associated with low permeability.  
 37 Understanding the processes involved in the migration of CO<sub>2</sub> in storages with low  
 38 permeability, influenced by the natural existence of fractures and faults in the ground, allows  
 39 selecting the best injection techniques that guarantee safe storage (Iding and Ringrose, 2010).  
 40 The interactions that occur between CO<sub>2</sub>-brine-rock in saline aquifers can have effects on their  
 41 stability (Phuc Vu et al., 2018) and tightness, resulting more or less favorable for CO<sub>2</sub> storage  
 42 (Le Gallo and de Dios, 2018).

43 The secondary porosity developed in a storage is the result of mechanical processes:  
 44 compaction, plastic and brittle deformation, fracturing; and geological ones: dissolution,  
 45 precipitation, volume reductions by mineralogical changes (Schön, J. H., 2015). As in the oil  
 46 industry, the injection and production of fluids can be improved by increasing secondary  
 47 porosity with fracking techniques that allow the interconnection of the pores through  
 48 processes of hydraulic fracturing (Yan et al., 2015) or fracture acidizing (Portier et al., 2007).

49 The use of scCO<sub>2</sub> as a non-aqueous fracturing fluid to increase the production of hydrocarbons  
 50 in oil and gas fields decreases the necessary water resources. It is presented as a safer option  
 51 regarding the use of acids by decreasing the required injection pressure, with greater  
 52 formation stability and less environmental impact. ScCO<sub>2</sub> for the production of hydrocarbons  
 53 presents (Middleton et al., 2015), among other advantages, an increase in the generation and  
 54 propagation of fracturing with a lower injection rate, being able to generate more extensive  
 55 and complex fracture networks than water-based working fluids. The use of scCO<sub>2</sub> against  
 56 water enables a greater development of fractures, the permeability of fractured rocks  
 57 increases with fracturing with scCO<sub>2</sub>, resulting in three orders of magnitude higher than  
 58 traditional hydraulic fracking. Furthermore, in the presence of shale, water can alter the  
 59 mechanical properties of clay-rich shale reservoir formations, reacting with minerals and  
 60 closing the fractures created during the fracturing operation, reducing the stimulation  
 61 efficiency (Yunzhong et al., 2018).

62 Acidizing is one of the most effective and widely means used of oil and gas operators to  
 63 stimulate well productivity (Yuan et al., 2015; Hong et al., 2017; Liqiang et al., 2017; Li et al.,

64 2015; Folomeev et al., 2014; Carpenter N.F., 1962). Commonly, it is undertaken in new wells to  
65 maximize initial productivity, and in old ones to restore the recovery of energy resources.  
66 Although the type of formation will determine the acids that must be used, their permeability  
67 influences the pressure required for pumping (American Petroleum Institute, 2014).

68 The study of the fractured rock massifs permeability has been carried out by means of on-site  
69 measurements, laboratory tests, theoretical derivation and numerical simulation. Using high-  
70 pressure injection tests to characterize the hydraulic properties of fractured rock strata (Chen  
71 et al., 2015b).

72 With the injection of CO<sub>2</sub> in the geological formations the balance of the system is altered,  
73 where once CO<sub>2</sub> is dissolved in the formation fluid two processes can be developed: the  
74 solubility trapping (Abba et al., 2019) and the mineral trapping. In the first, with a decrease in  
75 pH, CO<sub>2</sub> is trapped in its ionic species (CO<sub>3</sub><sup>2-</sup> and H<sup>+</sup>), taking place the dissolution of the oxides  
76 and carbonates on a time scale of days/weeks, which may produce variations in porosity and  
77 permeability (Kampman et al., 2014, Lamy-Chappuis et al., 2013). In the second, these  
78 reactions increase the alkalinity of the CO<sub>2</sub>-brine mixture, generating the subsequent  
79 precipitation of carbonates on a weeks/months time scale (Kampman et al., 2014). This  
80 phenomenon facilitates the geochemical interaction between the formation fluids, the storage  
81 rock and the seal rock (Mitiku et al., 2013, Holzheid, 2016a), giving rise to the mineral trapping  
82 (Ketzer et al., 2009, Soong et al., 2004).

83 During the CO<sub>2</sub> sequestration, the saturated brine dissolves the intergranular cement,  
84 producing a detachment and entrainment of fines in the direction of flow, by injection or by  
85 the interfacial forces acting on the particles at the CO<sub>2</sub>-brine interface (Othman et al., 2018b).  
86 The interfacial force that is a function of wettability is determined both by the mineralogy of  
87 the storage (Zhang, X. et al., 2020) and by the state (gas, liquid or supercritical) in which the  
88 CO<sub>2</sub> is injected (Peysson et al., 2014; Valle, L.M. et al., 2018).

89 The relationship between the permeability and the pressure drop allows predicting the  
90 injection rate in the aquifer and, where appropriate, the productivity of the reservoir. To know  
91 the existence of permeability in a formation, it is necessary to establish an injection or  
92 production flow with a constant pressure drop. The presence of interconnected pores allows  
93 the fluids to flow (Tongjun et al., 2015, Landau et al., 1987, Nazridoust et al., 2006), otherwise  
94 fluctuations or pressure peaks occur due to the absence of effective porosity or the existence  
95 of preferential channels that can change due to the drag of fines. In the injection process into  
96 the reservoir, the mineral particles present can be detached, being suspended in the injected  
97 fluid and, when their size allows, strain in the pore throats during transport. This results in a  
98 significant decrease in the permeability of the porous medium due to the process known as  
99 fines migration, which can significantly influence the capacity of the injection wells by  
100 supplying fluid to the reservoir.

101 The negative effect of fines migration on the formation permeability is one of the physical  
102 mechanisms that most affect wells (Russell et al., 2017; Khilar and Fogler, 1998; Civan, 2007;  
103 Farajzadeh et al., 2016), oil wells (Barkman et al., 1975; Zeinijahromi et al., 2016), gas wells  
104 (Byrne and Wagoner, 2009) and surface aquifers of drinking water (Prommer et al., 2013).

105 Several laboratory studies show a decrease in permeability with high injection/production flow  
106 rates (Khilar and Fogler, 1998; Zheng et al., 2014; Russell et al., 2018) because the drag force  
107 generated causes the migration of the adhered fines and the decrease in production and  
108 injectivity in high ratio wells. Operations carried out in a porous medium containing fine  
109 particles susceptible to detachment or entrapment are potentially prone to fines migration.

Directional permeability in natural fractured networks is significantly dependent on the geomechanical properties of fractures (Richeng et al., 2016). The preferential flow paths that develop despite their relatively low matrix permeability are governed by the characteristics of the connected fracture networks (Chen et al., 2015 a).

Pore scale tests on the migration of fines in sandstone samples, during the interaction of saturated brine with scCO<sub>2</sub>, generate permeability drops of around 15% -30% (Sayegh et al., 1990; Dawson et al., 2015; Pudlo et al., 2015). Static injection experiments varying the chemical composition of the brine have confirmed that most of the sandstone minerals in the storage formation and those of the seal rock can be mobilized and dissolved in the presence of scCO<sub>2</sub> saturated brine (Jean et al., 2015).

This work investigates the effectiveness of the injection of scCO<sub>2</sub> enriched brine in two limestone and dolomite formations that present natural fracturing, capable of constituting a CO<sub>2</sub> store. This action modifies the petrophysical parameters of porosity and permeability and ensures the injection into the aquifer without compromising the tightness of the storage in the long term, compared to the fracture acidizing methods used in the oil industry.

## 2. Materials and methods

### 2.1. Materials

The samples studied belong to a deep saline aquifer that can store CO<sub>2</sub>. The site represents structural dome where the pair seal-reservoir is located within Jurassic Formation (Marly Lias and Sopeña respectively) (de Dios et al., 2018). Overburden is formed of Dogger, Purbeck and Weald and the underlying seal is located at Triassic Keuper (Rubio et al., 2014). Reservoir is Sopeña Formation (120 m thick) comprised of limestone at its upper part and dolomites at the bottom (Kovács, 2014). The storage rock consists mainly of carbonates comprising the geological formations (Fd), Sopeña Calizo (SC) and Sopeña Dolomítico (SD). A well that crosses the seal and the storage, allows to extract, parallel to bedding, six samples located at a depth around 1500 m. Table 1 shows their characteristics, dimensions and porosity (measured in AccuPyc II 1340 Pycnometer).

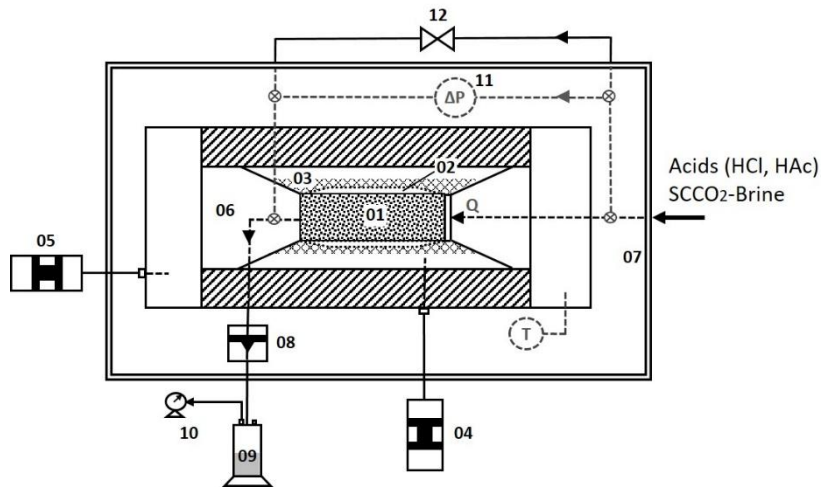
Table 1. Dimensions and porosity of the samples.

Sample ID	F <sub>d</sub>	Depth (m)	Weight (g)	Length (mm)	Diameter (mm)	Volume			Grain Density (g/cm <sup>3</sup> )	Porosity (%)
						Total (cm <sup>3</sup> )	Solid (cm <sup>3</sup> )	Pore(cm <sup>3</sup> )		
A1	SC	1448.3	204.42	67.41	37.90	76.03	75.86	0.17	2.69	0.22
A2	SC	1449.7	218.31	71.87	37.84	80.82	80.36	0.45	2.71	0.56
A3	SD	1518.5	217.61	72.24	37.86	81.31	76.61	4.69	2.84	5.77
A4	SC	1442.1	186.38	72.89	37.96	82.50	65.84	16.65	2.83	20.18
A5	SD	1525.7	230.39	74.06	37.82	83.20	81.28	1.91	2.83	2.30
A6	SC	1443.8	213.83	72.11	38.02	81.85	76.88	4.96	2.78	6.06

ID: sample identification; F<sub>d</sub>: geological formation Sopeña Calizo/Dolomítico (SC/SD)

The selection of the field samples in this research avoids the lack of correspondence between the results of the petrophysical tests carried out in analogues and those coming, as in this case, from materials in depth (Wang et al., 2013).

Each rock samples, previously saturated in brine and placed in the triaxial cell in the ATAP experimental facility (Valle and Martínez, 2105) (Fig. 1), was subjected to one of the injections of HCl, HCl-Acetic (CH<sub>3</sub>COOH) and Brine-scCO<sub>2</sub> mixture, respectively. During the test, the pressure and temperature conditions, characteristic of the aquifer under study as well as the concentrations of the fluids that will be injected into the samples, were established (American Petroleum Institute, 2014).



148

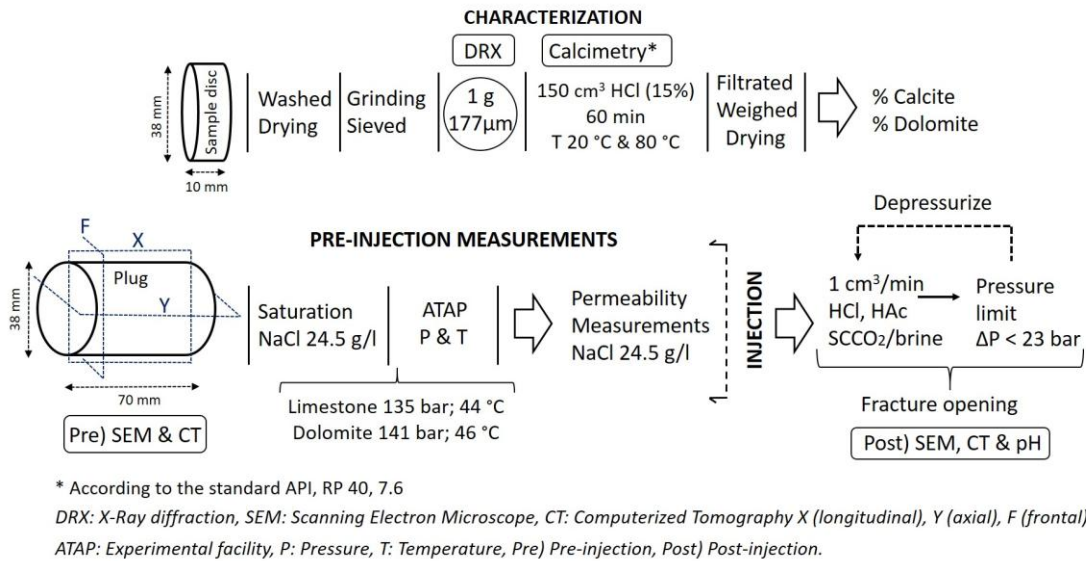
149 **Fig. 1.** Experimental ATAP system (Valle and Martínez, 2015): Rock sample (01), Thermo-shrinkable  
 150 Sleeve (02), Viton sleeve (03), Radial pump to confine glycerin (04), Axial pump to confine glycerin  
 151 (05), Axial piston (06), Controlled temperature oven (07), Back pressure, BPR (08), Separator (09),  
 152 Gasometer (10), Pressure difference (11), and Bypass (12).

153 The sample (01), saturated in brine, is covered with a thermo-shrinkable plastic (02), which  
 154 prevents the diffusion of CO<sub>2</sub> towards the radial confinement glycerin. On the outer viton  
 155 sleeve (03), using the hydraulic group with glycerin (04), the radial confining pressure is  
 156 established. With the axial hydraulic group (05), the glycerin pressure is increased, which  
 157 causes the displacement of the piston (06) generating the axial stress. In this way, a triaxial  
 158 confining pressure is established in the rock-fluid system corresponding to the depth of the  
 159 samples. The oven (07) and the back-pressure equipment (08) maintain respectively a  
 160 temperature of 31 °C and a pore pressure above 74 bar, conditions ensure that CO<sub>2</sub> is in the  
 161 supercritical state throughout the test. The test fluids are collected at the outlet in the  
 162 separator (09) under atmospheric conditions, where the volume of the liquid is measured, and  
 163 CO<sub>2</sub> gas is separated and sent to the gasometer (10) to measure its volume. A membrane type  
 164 sensor (11) measures the incremental pressure ( $\Delta P$ ) between the injection and production  
 165 surface of the sample. When the pressure sensor limit of 23 bar( $\Delta P$ ) is reached, the bypass  
 166 valve (12) opens, allowing the system to be depressurized, preventing injection fluid from  
 167 passing through the sample, connecting directly to the production line.

168 The data of the tests are recorded and subsequently interpreted using numerical models  
 169 (Lenormand et al., 1988) in the settings made with the Cydar™ software (Lenormand, 2012).

## 170 **2.2. Methodology**

171 The study of the material from both formations, carried out in the laboratory, includes a  
 172 previous characterization stage. A plug is drilled from each of the 6 samples and the end trims  
 173 are preserved. Of these end trims, a disc corresponding to the injection surface (sample disc) is  
 174 used for the mineralogical characterization of the sample (Fig. 2 characterization) and the plug  
 175 is used for petrophysical characterization (Fig. 2 pre-injection measurements) and injection  
 176 tests (Fig. 2 injection).



178 **Fig. 2.** Diagram of characterization tests, pre-injection measurements and injection into samples.

179 **2.2.1. Disc characterization**

180 A disk with dimensions of approximately 10x38 mm corresponding to injection surface of each  
 181 sample is washed, dried, grinded and sieved, and then analyzed by XRD and calcimetry tests  
 182 (20/80 °C), to determine its mineralogy and its percentage contents of calcite and dolomite  
 183 (Fig. 2 characterization).

184 The major mineral compounds present on the surface, where the injection of each sample is  
 185 carried out (injection surface), were determined (rough determination) using XRD (Table 2).  
 186 The geological host formation of the samples, SC or SD, does not determine its principal  
 187 content in calcite or dolomite, in both cases varying its proportions, and even as in the case of  
 188 the sample A4 (SC) no calcite content is detected close to the injection surface.

189 **Table 2.** Major mineral compounds of the injection surface. XRD

Sample ID	Ca	Calcite	Dolomite	Quartz	Anhydrite
F <sub>d</sub>	CaCO <sub>3</sub> (%)	CaMg (CO <sub>3</sub> ) <sub>2</sub> (%)	SiO <sub>2</sub> (%)	CaSO <sub>4</sub> (%)	
A1	SC	91.6	7.6	0.7	-
A2	SC	55.5	4.1	3.5	-
A3	SD	-	95.1	0.1	4.8
A4	SC	-	99.1	0.9	-
A5	SD	-	90.5	0.2	9.3
A6	SC	19.9	79.6	0.5	-

190 *ID: sample identification; F<sub>d</sub>: geological formation Sopeña Calizo/Dolomitico (SC/SD)*

191 The calcimetry or solubility test to the acid (API standard, RP 40, 7.6) determines  
 192 gravimetrically the sensitivity of the formation to react with acid. The results are used to  
 193 determine the volumes of acids required in the field to ensure success in acid stimulation and  
 194 damage transmitted to the formation (American petroleum Institute, 2014).

195 **Table 3** shows the partial and final results of the calculations corresponding to the calcite and  
 196 total carbonate content of the samples.

200 Table 3. Percentage in calcite and total carbonate of the samples.

Sample		W <sub>s</sub> (g)		W <sub>s</sub> + dry filter (g)		Calcite %	Carbonate %
ID	F <sub>d</sub>	20 °C	80 °C	20 °C	80 °C	20 °C	80 °C
A1	SC	1.022	1.016	0.149	0.148	93.83	93.89
A2	SC	1.040	1.087	0.171	0.168	91.82	92.08
A3	SD	1.057	1.100	0.101	0.097	98.48	98.90
A4	SC	1.009	1.004	0.126	0.125	86.85	95.80
A5	SD	1.010	1.069	0.112	0.111	97.33	97.47
A6	SC	1.094	1.090	0.154	0.153	90.42	91.75

According to the standard API, RP 40, 7.6

ID: sample identification; F<sub>d</sub>: geological formation Sopeña Calizo/Dolomítico (SC/SD); W<sub>s</sub>: sample weight

201

### 202 2.2.2. Plug characterization

203 A cylindrical plug with dimensions of approximately 70x38 mm, which is washed to remove its  
204 content in brine and/or drilling mud, is obtained from each sample in the pre-injection stage  
205 (Fig. 2 pre-injection).

206 The injection surface is studied using Scanning Electron Microscopy with Energy Dispersive X-  
207 Ray Spectroscopy (SEM-EDX) in the positions of interest that present visible open/filled  
208 fissures to the naked eye or changes in mineralogy. After drying it in an oven and measuring its  
209 porosity, different points are selected within the determined position to run SEM for obtaining  
210 high and low-magnification images and its spectra with EDX. The precise positions of the plugs  
211 are fixed (longitudinal X (19 mm), axial Y (19mm) and frontal F (injection surface) sections). The  
212 surface and the interior of the sample are analyzed by Medical Computed Tomography (CT)  
213 (Somatom-Siemens Sixteen-row multislice spiral, cutting thickness 0.6 mm with reconstruction  
214 increments 0.1 mm; FOV 50 cm, 20-345 mA and 80, 110, 130 Kv) prior to injection (Fig. 2 pre-  
215 injection).

216 Both SEM and CT studies are repeated on the positions fixed in the plugs after the acid and  
217 scCO<sub>2</sub>-brine mixture injections, observing changes and evolution of the fissures (Fig. 2  
218 injection).

### 219 2.2.3. Pre-Injection

220 The plugs, once they are characterized, are saturated in brine (24.5 g/l) and placed in the ATAP  
221 device, where conditions corresponding to the depth of the formation, the confining pressure  
222 (135/141 bar) and temperature (44/46 °C), are set. Under these conditions, the sample  
223 undergoes the injection process (Fig. 2 pre-injection). Its permeability, k (mD), to liquid (brine  
224 with the same conditions) is measured using Darcy's Law in laboratory units [q (cm<sup>3</sup>/s), A (cm<sup>2</sup>),  
225 μ (cP), L (cm) y ΔP (bar)] (Soulain, 2015; Agnaou, 2017; Wang and Reed, 2009; Zhao et al.,  
226 2011), which is expressed according to Eq. 1.

$$227 \quad K = \frac{q}{A} \cdot \frac{\mu \cdot L}{\Delta P} \quad (1)$$

228 Darcy's Law for a single phase and steady state radial flow through a porous medium, in field  
229 units [v(ft/s), q (bbl/day), A (ft<sup>2</sup>), K (D), μ (cP), dP (psi), dr (ft)], is expressed according to Eq. 2.

$$230 \quad v = \frac{q}{A} = -1.127 \cdot \frac{K}{\mu} \cdot \frac{dp}{dr} \quad (2)$$

231 According to experience, the relationship between permeability K (D) and pore pressure P<sub>p</sub>  
232 (psi) can be established (Al-Award, 2001), consistent with Eq. 3.

$$233 \quad K = a_0 + a_1 \cdot P_p + a_2 \cdot P_p^2 + a_3 \cdot P_p^3 + \dots \quad (3)$$

234 Joining equations 2 and 3, and integrating (Fig. 3), we can arrive at the expression of Eq. 4 (Al-  
235 Award, 2001).

$$\int_{r_1}^{r_2} \left[ \frac{q}{2 \cdot \pi \cdot r \cdot h} \right] \cdot dr = \frac{1.127}{\mu} \cdot \int_{P_{p1}}^{P_{p2}} [a_0 + a_1 \cdot P_p + a_2 \cdot P_p^2 + a_3 \cdot P_p^3 + \dots] \cdot dp \quad (4)$$

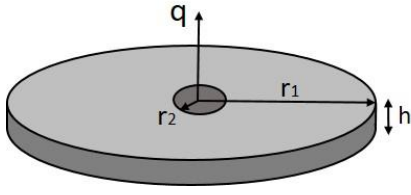


**Fig. 3.** Diagram of radial flow to the producer/injector well.

Therefore, two expressions can be derived for the fluid flow. Firstly, by taking into account the permeability pore pressure relationship Eq. 5:

$$q = \frac{7.081 \cdot h \cdot \Delta P_p}{\mu \cdot \ln\left(\frac{r_1}{r_2}\right)} \cdot \left[ a_0 \cdot P_p + \frac{a_1}{2} \cdot P_p^2 + \frac{a_2}{3} \cdot P_p^3 + \frac{a_3}{4} \cdot P_p^4 + \dots \right] \frac{P_{p1}}{P_{p2}} \quad (5)$$

Secondly, by neglecting permeability-pore pressure relationship. Establishing a relationship between the injectivity/productivity  $q$  (bbl/day) and the pore pressure  $P_{p1}$  (psi) and  $P_{p2}$  (psi) existing far  $r_1$  (ft) and near the well  $r_2$  (ft), respectively (Fig. 3), expressed as the Eq. 6:

$$q = \frac{7.081 \cdot K h \Delta P_p}{\mu \ln\left(\frac{r_1}{r_2}\right)} \quad (6)$$

The difference between the well pressure ( $P_{p2}$ ) and the mean pressure of the reservoir fluids ( $P_{p1}$ ) is one of the fundamental processes that govern the movement of fluids in the reservoir. This process tends to increase the amount of fluids produced, or what is the same in the case of CO<sub>2</sub> storages, the fluids injected into the aquifer.

If fluid flows through fractures is assumed to be laminar flow, the flow rate along the flow direction through a fracture can be described by the famous “cubic law” (Tongjun et al., 2015; Landau and Lifshitz, 1987; Nazridoust et al., 2006) Eq. 7:

$$q = \frac{f_a^3 \cdot l \Delta P}{12 \mu l_0} \quad (7)$$

Absolute permeability is a variable in all flow equations, therefore, for its correct estimation, it must be expressed in these equations as a function of effective overburden pressure (the difference between overburden pressure and reservoir pore pressure) (Chen et al., 2015b).

An accurate permeability-effective stress ratio can be determined using a tri-axial compression cell capable of generating pore pressure and axial and radial stress (Fig. 1).

#### 2.2.4. Injection

Once the injection of brine into the sample has been carried out, the continuous injection of acid mixtures and scCO<sub>2</sub>/brine is carried out at a constant flow rate of 1 cm<sup>3</sup>/min. This flow rate is selected due to the low absolute permeability and the size of the samples (10 times the diameter of the samples from the study by Al-Khulaifia et al., 2018). The injection process was performed continuously compared to the batch injection by Holzheid, 2016b. The composition of the mixtures injected into each sample is shown in Table 4.

Table 4. Type of injection in each sample.

Sample	Injection mixture
A1 (SC)	10 % HCl
A2 (SC) & A3 (SD)	15 % HCl
A4 (SC)	10 % HCl & 10 % Acetic (CH <sub>3</sub> COOH)
A5 (SD) & A6 (SC)	50 % scCO <sub>2</sub> & 50 % brine

267

268 The incremental pressure between the injection-inlet/production-outlet surfaces is registered.  
 269 Production is verified through the flow line downstream of the core holder that guides the  
 270 fluids to the separator, thereby ensuring the circulation of fluids through the sample. When  
 271 the maximum of the differential pressure sensor (23 bar) is reached, the injection is stopped  
 272 and the system is depressurized by opening the bypass valve. The process is repeated as many  
 273 times as necessary until fluid production is achieved.

### 274 3. Tests and results

#### 275 3.1. Pre-injection measurements

276 During the brine injection into the samples (NaCl 24.5 g/l) at the fixed flow rates (0.2, 0.5 and 1  
 277 cm<sup>3</sup>/min) very high pressures are reached, which, however, cannot stabilize the differential  
 278 pressure. The low production of brine with an unstable incremental pressure and above the  
 279 limit of the pressure sensor, indicates in all cases that the absolute permeability (K) is less than  
 280 0.1 mD.

#### 281 3.2. Injection process

282 The injection of acid mixtures through the samples (Table 4) was carried out within the  
 283 experimental ATAP system (Fig. 1 and Fig. 2 injection). Figures 4-7 show the records of the  
 284 pressure sensors (P<sub>inj</sub>, ΔP) obtained during the entire injection process at a constant flow rate  
 285 of 1cm<sup>3</sup>/min until, if it happens, reaching the limit of the differential pressure (23 bar). The  
 286 injection process is stopped at that moment and the system is depressurized by opening the  
 287 bypass.

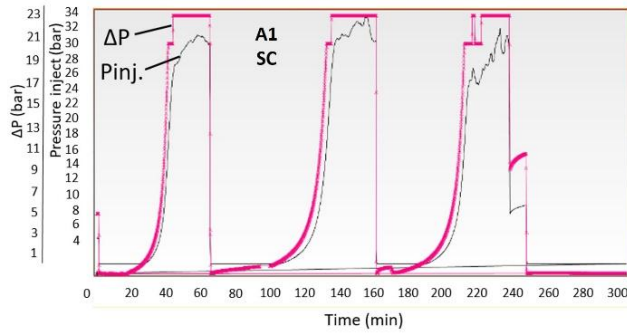
288 It was not possible to stabilize the pressure drop (ΔP) in any of the samples, probably because  
 289 the existing micro-cracks act as preferred pathways. As stated in Eq. 7 there is proportionality  
 290 between the pressure drop in the fissures and the injected flow that circulates through them.

##### 291 3.2.1. Injection pressure evolution results

###### 292 10% HCl and 15% HCl injections

293 In sample A1 (SC), the 10% HCl injection was carried out for three cycles until a maximum  
 294 injection pressure of 34 bar was reached in the second cycle, with pressure fluctuations due to  
 295 internal circulation of part of the acid. The injection pressure is maintained in a similar range in  
 296 the three injection cycles with the exception of the last cycle, where it drops to 9 bar with a  
 297 small production of acid (Fig. 4).

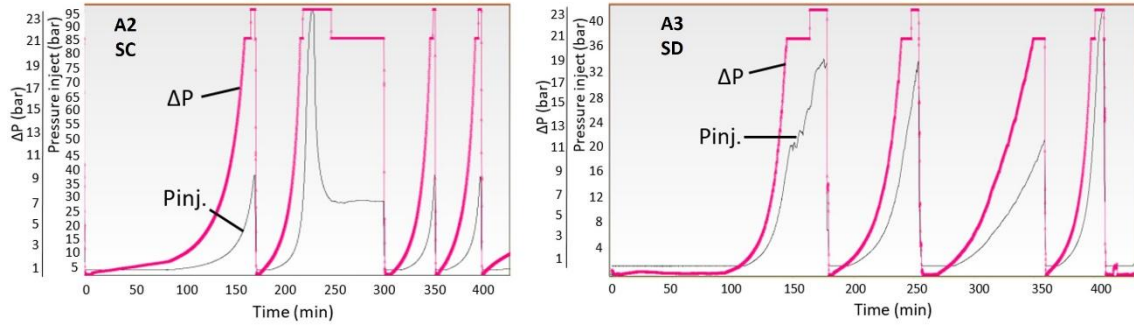
298 In samples A2 (SC) and A3 (SD), the injection of 15% HCl is carried out for 4 cycles in both  
 299 cases. The injection pressure in sample A2 (SC) reaches a peak of 95 bar in the second cycle,  
 300 probably due to the momentary collapse of the injectivity due to the clogging of the pores (Eq.  
 301 7), keeping the rest around 35 bar. On the other hand, in sample A3 (SD) the injection pressure  
 302 reached in the first two cycles is 32 bar, with a decrease to 20 bar in the third cycle, after an  
 303 improvement in the sample's injectivity, and an increase up to 42 bar in the fourth one due to  
 304 the collapse of such injection (Fig. 5).



305

306

**Fig. 4.** Injection of 10% HCl (A1).



307

308

**Fig. 5.** Injection of 15% HCl (A2, A3).

309

**HCl 10% and Acetic, CH<sub>3</sub>COOH 10% injections**

310

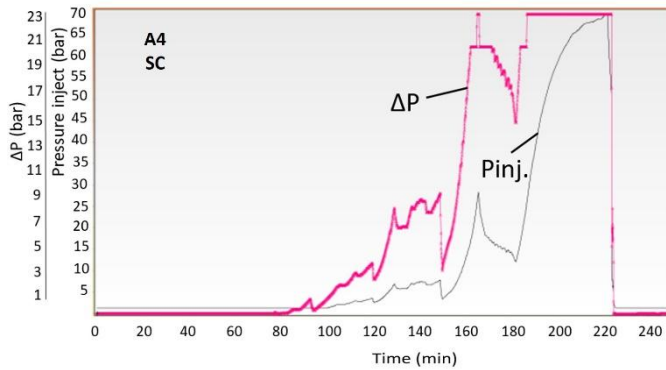
311

312

313

314

The injection of the mixture 10%/10% HCl/Acetic was carried out in sample A4 (SC). The injection has a constant low pressure for more than 60 minutes, and a subsequent rise with fluctuations until reaches the injection collapse at 70 bar and 220 min. Since injection has been possible without reaching the limit of the pressure sensor during this time, once it is reached the system is depressurized and no new injection is performed (Fig. 6).



315

316

**Fig. 6.** Injection of HCl 10% and HAc 10% (A4).

317

**scCO<sub>2</sub> 50% and brine 50% injections**

318

319

320

In samples A5 (SD) and A6 (SC) the injection of the mixture 50%/50% scCO<sub>2</sub>/brine was carried out with a back pressure adjustment (BPR) and an offset pressure of the system at 74 bar ensuring the maintenance of the supercritical conditions.

321

322

323

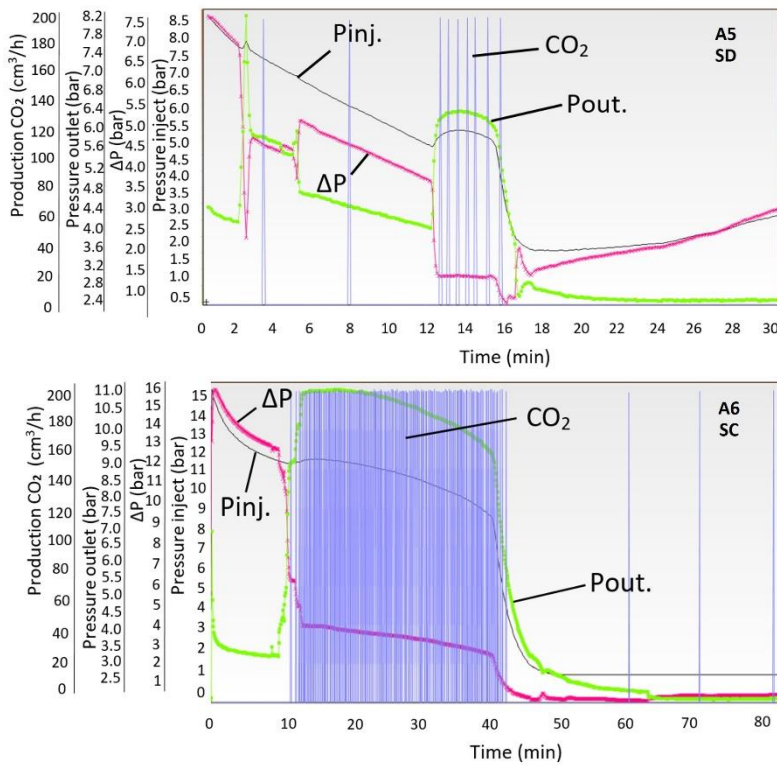
324

With the injection of the scCO<sub>2</sub>/brine mixture, the pressure sensor limit is not reached in any of the tests carried out on each of the samples. Therefore, it is not necessary to depressurize the system at any time. In addition, the injection pressures reached a maximum of 8.5 bar (relative, offset) in sample A5 (SD) and 15 bar (rel, offset) in sample A6 (SC), with a progressive

325 decrease until the beginning of CO<sub>2</sub> production (10 min after starting the injection). At this  
 326 time a slight rise in pressure occurs, to decrease slightly as the scCO<sub>2</sub>/brine mixture passes  
 327 through the sample.

328 The continuous decrease in pressure from the start of the injection without the presence of  
 329 peaks confirms that there is circulation of the mixture through the sample without collapse of  
 330 the pores (Fig. 7).

331 The CO<sub>2</sub> production is measured on the gasometer (Fig. 1. 10) located after the production  
 332 fluid collector or separator (Fig. 1. 09). As this collector is located after the back pressure valve  
 333 (Fig. 1. 08), it receives the fluids at atmospheric pressure, so the scCO<sub>2</sub>/brine mixture separates  
 334 into the liquid phase (brine) that remains in the collector and is measured by calibrated  
 335 burette. The gas phase (CO<sub>2</sub>) exits through the upper part of the separator and reaches the  
 336 gasometer where the volume produced is measured and recorded.



337  
 338 **Fig. 7.** Injection of brine 50% and SCCO<sub>2</sub> 50% (A5 and A6).

339 **3.2.2. SEM and CT results**

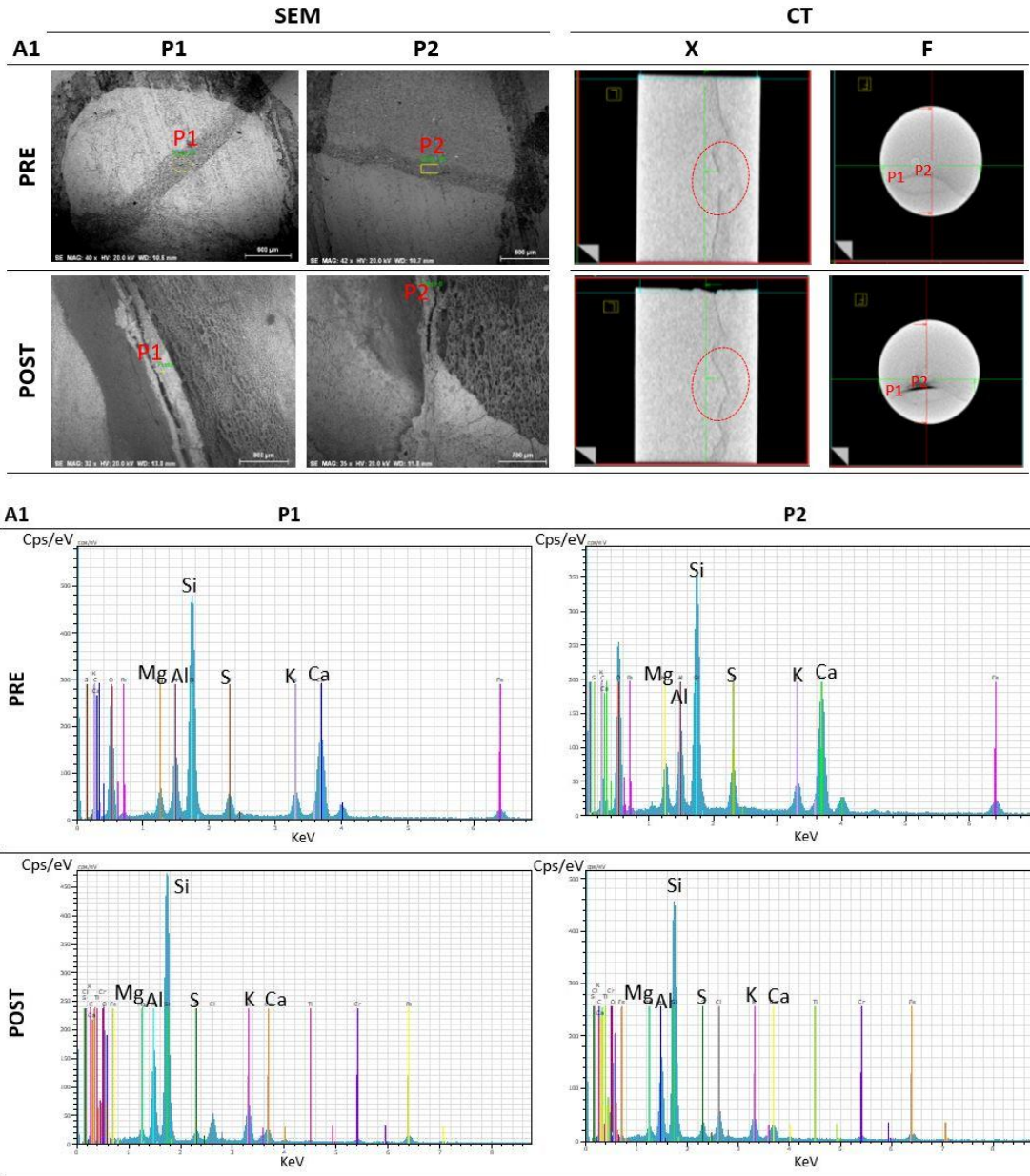
340 The SEM and CT images (X: longitudinal, Y: axial and F: frontal; Fig. 2) before and after the acid  
 341 and scCO<sub>2</sub>/brine mixtures pass through the samples, allow us to observe the effects and the  
 342 changes they produce in them.

343 **10% HCl and 15% HCl injections**

344 SEM-EDX images of sample A1 (SC) indicate that mineral dissolution has occurred around the  
 345 potassium aluminosilicates and quartz filling the fissures. The spectra of positions 1 and 2 (Fig.  
 346 8 EDX POST) indicate a decrease in calcium and magnesium, main components of the matrix  
 347 (Table 2), produced by the dissolution of the carbonates. This superficial dissolution is verified  
 348 in the frontal section (F) of the images obtained by CT, showing in the longitudinal section (X)  
 349 an interconnection of the fissures in the interior areas of the sample (Fig. 8 CT red circles).

350 The released quartz grains, less soluble in acid, together with the aluminosilicates are  
 351 entrained by the injection flow causing the increase and fluctuations of the injection and  
 352 incremental pressures.

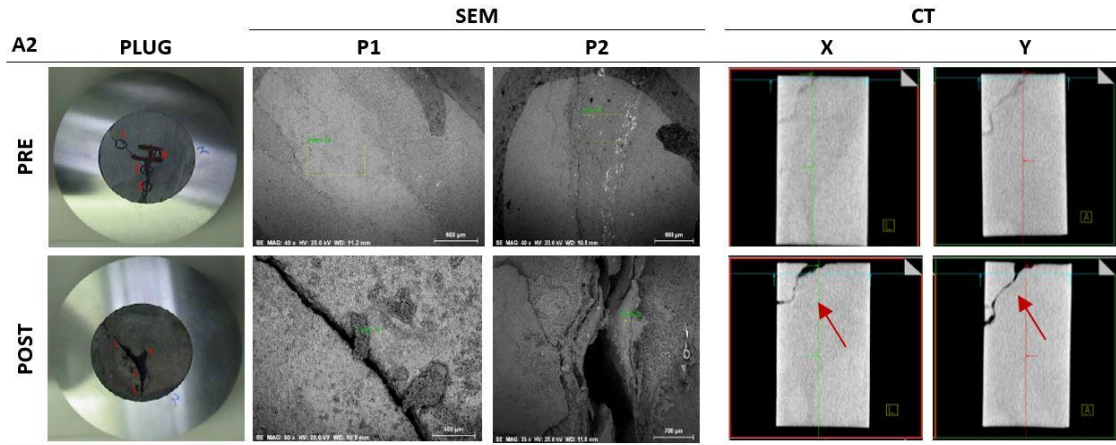
353 Fine entrainment seems to decrease in the last injection cycle as there is a decrease in  
 354 pressure ( $P_{inj}$ ,  $\Delta P$ ), produced at 240 min (Fig. 4), linked to the production of mixture in the  
 355 separator. This is when a natural injection process is established through the sample,  
 356 presumably through the interconnected fissures.



358  
 359 **Fig. 8.** SEM, EDX (injection surface) and CT sample A1 previous (PRE) and subsequent (POST) to the  
 360 injection.

361 The sample A2 (SC) shows fissures filled with potassium and quartz aluminosilicates on its  
 362 surface (Fig. 9 SEM P1 & P2-PRE), producing after injection a decrease in calcium and  
 363 magnesium, major components of the matrix. The EDX obtained are similar to those of sample  
 364 A1 (SC), so they have not been included. The potassium aluminosilicates embedded in the  
 365 matrix will be free but not dissolved (P1) or partially dissolved (P2) (Fig. 9 SEM POST), as

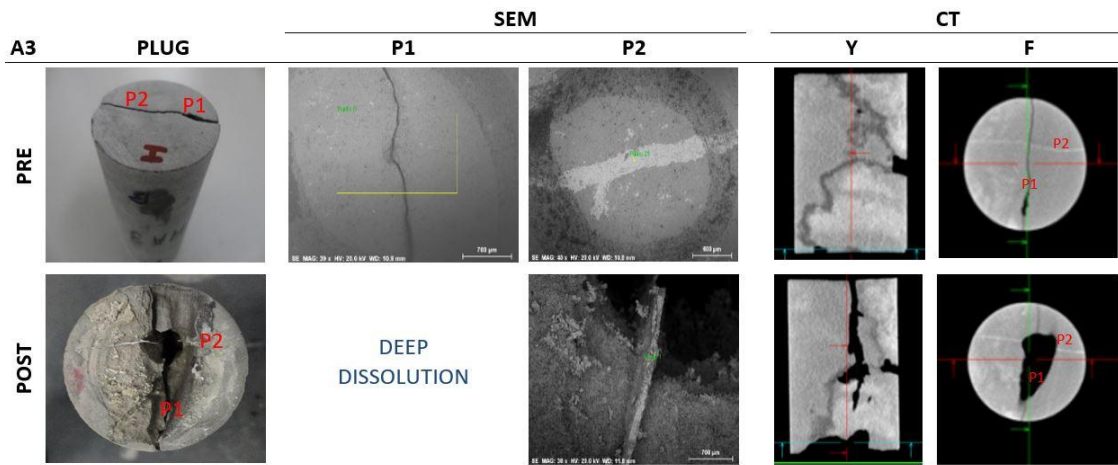
366 confirmed by CT images (Fig. 9 CT POST red arrows). The increased in injection and  
 367 incremental pressures confirm the entrainment of potassium aluminosilicate fines by the  
 368 acidic injection stream (Fig. 5).



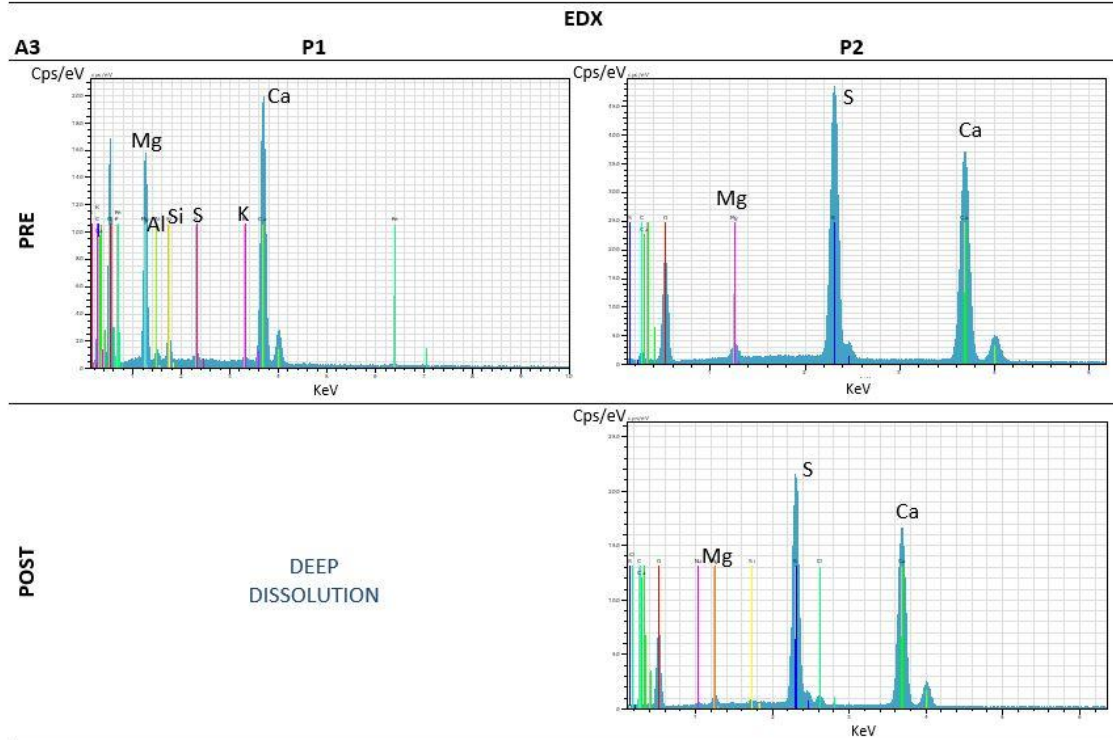
369  
 370 **Fig. 9.** SEM, EDX (injection surface) and CT sample A2 previous (PRE) and subsequent (POST) to the  
 371 injection.

372 In the sample A3 (SD), the absence in a fissure of resistant fillers such as silicates, anhydrite  
 373 and quartz results in a greater dissolution of carbonates (P1, with high content of calcium and  
 374 magnesium) (Fig. 10 EDX P1-PRE). Due to the high dissolution produced (Fig. 10 PLUG POST) it  
 375 was not possible to carry out the SEM study of this area after injection (Fig. 10 SEM P1-POST).  
 376 A high content of anhydrite has been detected, filling the fissure in position 2 (Fig. 10 EDX P2-  
 377 PRE), also observed in the XRD of Table 2. Its partial dissolution occurs after the dissolution of  
 378 the carbonates of the matrix (Fig. 10 EDX P2-POST).

379 The CT images (Fig. 10 CT Y-POST) show a longitudinal solution that crosses practically the  
 380 entire sample (enlarged fracture), through which the fine drag characteristic of both  
 381 fluctuations and increased in injection pressure has occurred (Fig. 5).



382



383

384 **Fig. 10.** SEM, EDX (injection surface) and CT sample A3 previous (PRE) and subsequent (POST) to the  
 385 injection.

386 ***HCl 10% and HAc 10% injection***

387 In the sample A4 with primary porosity (Table 1), a single injection with acid production from  
 388 the beginning was carried out. Although no open fissures are observed in the CT (Fig. 11 CT  
 389 PRE), the strong surface erosion observed (Fig. 11 PLUG POST) may be the cause of the  
 390 subsequent collapse produced by the dragging of solids, produced at 220 min (Fig. 6). This  
 391 dissolution and entrainment coincide both with its low initial pressure and with its fluctuations  
 392 and increases after the 60 min injection. After the initial dissolution and drag on the injection  
 393 face (Fig. 11 CT POST red arrow), it is observed that there is no subsequent dissolution due to  
 394 the collapse of the injection.

395 The spectrum of position 1 (lighter zone) (Fig. 11 SEM & EDX P1-PRE) indicates the presence of  
 396 chlorides (Cl) prior to injection (Fig. 11 EDX P1-PRE), causing its dissolution almost complete.  
 397 On the other hand, the scarce silica that has been initially detected, because it is scattered, has  
 398 been entrained in the solution produced by the acids (Fig. 11 EDX P1 & P2-PRE).

399 The erosion of the entire surface (Fig. 11 PLUG & CT POST red arrow) was originated during the  
 400 injection in A4, thus, spectra at positions 1 and 2 after injection have not been studied.

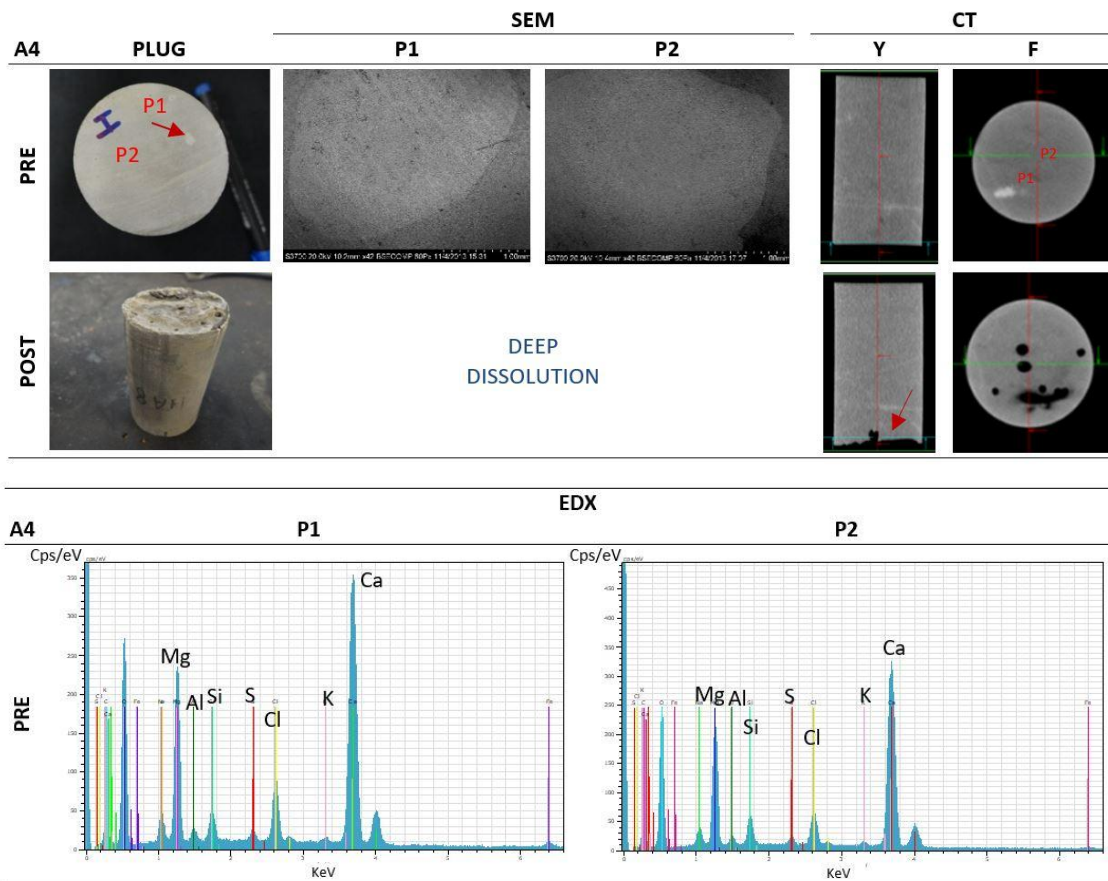


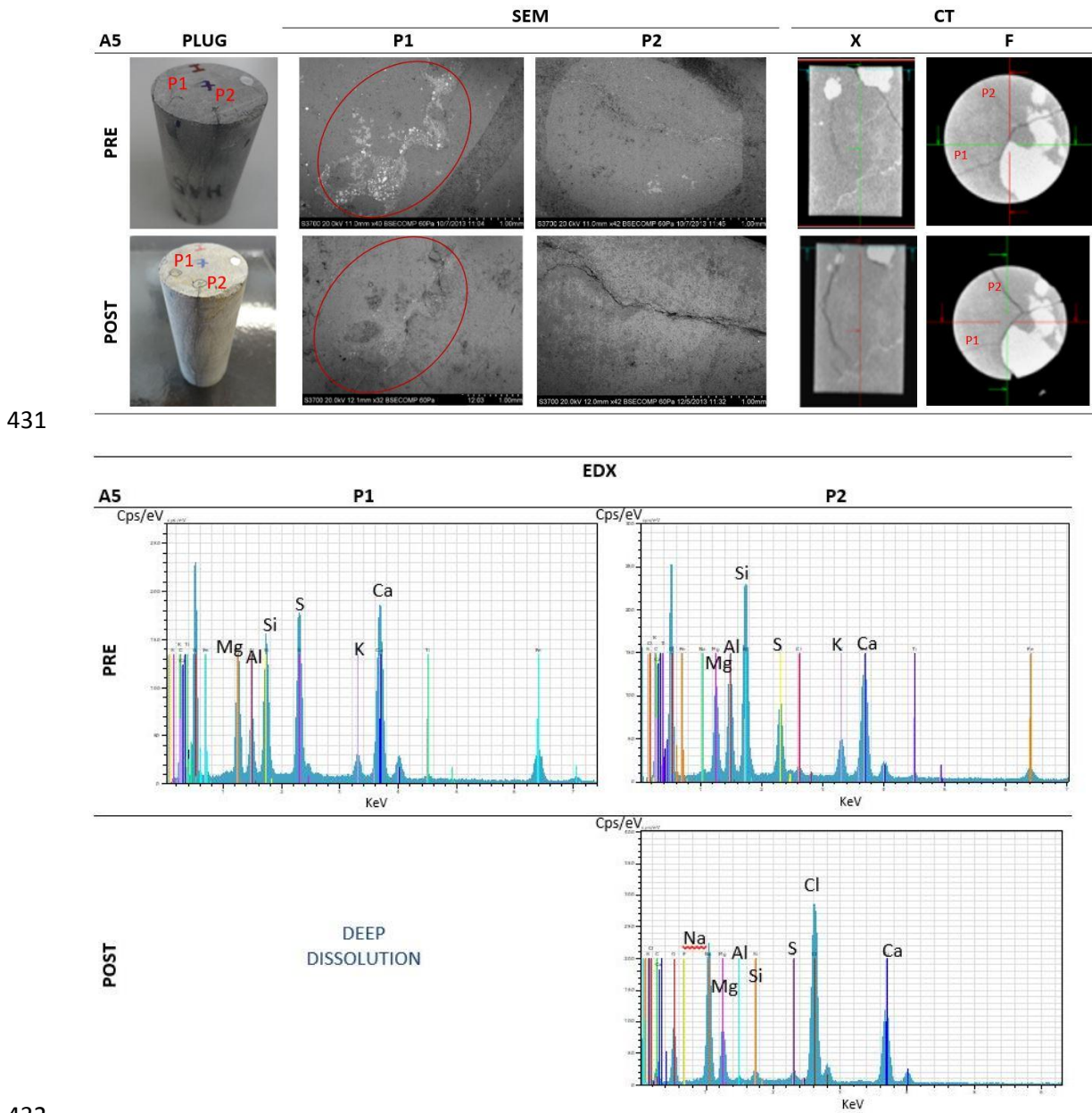
Fig. 11. SEM, EDX and CT sample A4 previous (PRE) and subsequent (POST) to the injection.

**scCO<sub>2</sub> 50% and brine 50% injections**

The SEM and CT images of the samples A5 (SD) and A6 (SC) do not present, except in position 2 (surface) of sample A5, fissure opening (Fig. 12 SEM P2-PRE). However, this solution has not produced solids entrainment since the injection pressure has decreased from the initial 8.5 bar, without fluctuations that indicate collapse, until the moment (at 12 min of injection) in which CO<sub>2</sub> and brine begin to be produced through the production surface (outlet) of the sample (Fig. 7). On the other hand, in the records of the injection pressure of scCO<sub>2</sub> enriched brine, the ΔP sensor limit is not reached, thus depressurizing of the system and stopping the injection was not necessary. The production of the mixture at the exit of the sample (production surface) begins within a few minutes of the injection without creating preferential pathways inside the sample and without producing the drag of solids that clog the production line increasing the pressure of the system.

The matrix of sample A5 is made up of carbonates, mostly dolomite, Table 2 (Fig. 12 EDX, PRE). The EDX at position 2 indicates magnesium and calcium concentrations (Fig. 12 EDX P2-PRE) similar to those in sample A4 (Fig. 11 EDX P1-PRE), however, less dissolution was observed with the scCO<sub>2</sub>/brine injection (Fig. 12 EDX P2-POST) than with HCl and Acetic (Fig. 11 PLUG POST). While the dolomite attack occurs (Fig. 12 EDX POST) the rest of the unaltered grains that are released are dragged away leaving open fissures and superficial holes (Fig. 12 SEM P1 & P2-POST). As a consequence of the presence in the sample of these hollow spaces (Fig. 12 SEM P1-POST red circles) the spectrum of position 1 post-injection could not be performed (Fig. 12 EDX P1-POST). The presence of residual iron sulfide grains identified as bright white dots, seems to indicate that the anhydrite (light gray area) that surrounds them had been generated as a consequence of its alteration (Fig. 12 SEM P1-PRE).

427 In position 2, the presence of silica in the fissure facilitates the dissolution of the surrounding  
 428 carbonates (Fig. 12 EDX P2-POST). Its effect is less than in the case of injection of HCl and  
 429 Acetic acids (Fig. 11 PLUG POST), also causing entrainment of non-soluble particles (silicates  
 430 and anhydrite).

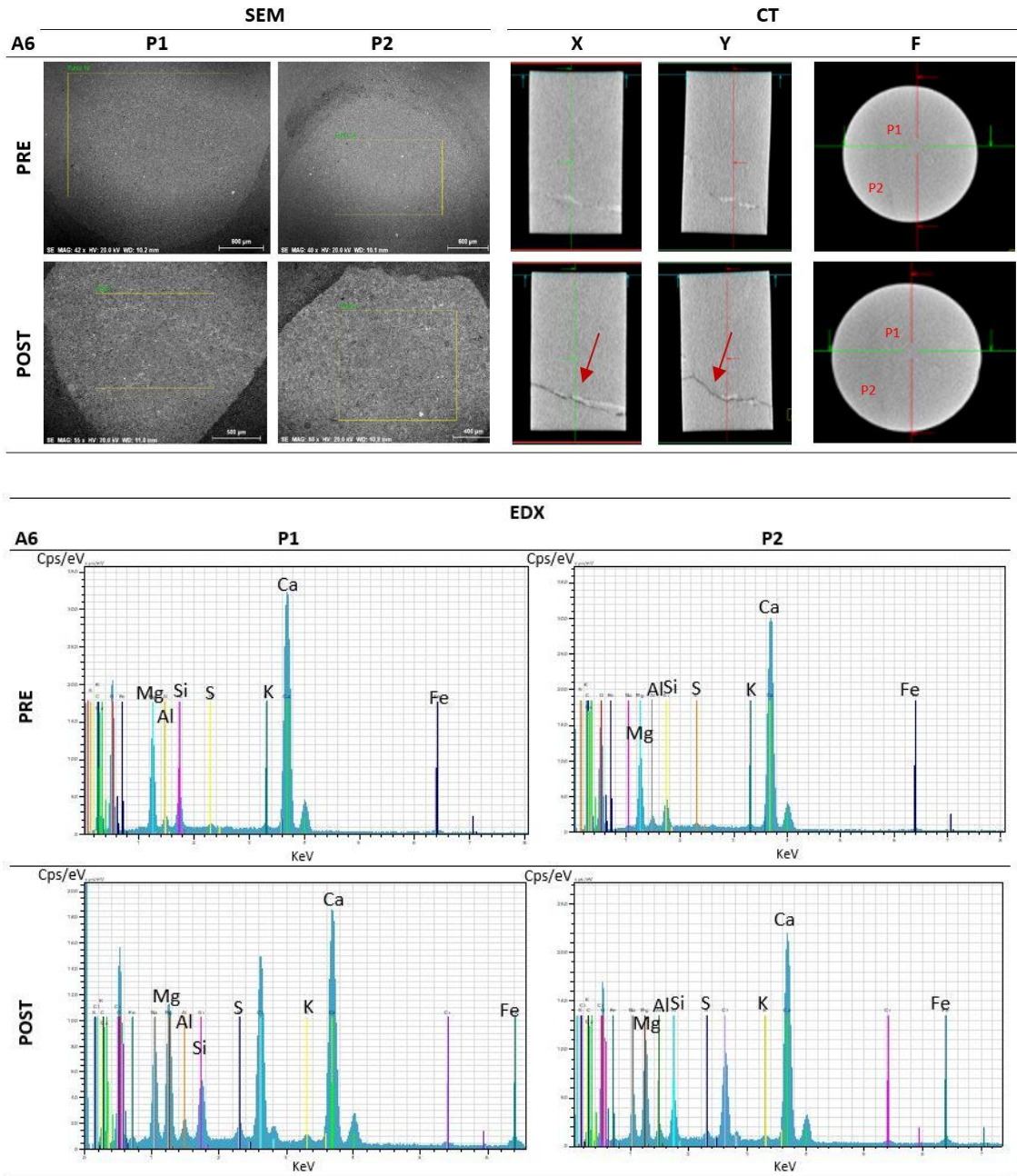


432  
 433 **Fig. 12.** SEM, EDX (injection surface) and CT sample A5 previous (PRE) and subsequent (POST) to the  
 434 injection.

435 The attack that occurs in sample A6 is lighter than in the other injections. The spectrum at  
 436 position 1 (Fig. 13 EDX P1-PRE) shows the presence of dolomite (DRX Table 2), with some iron  
 437 sulfides and silicates dispersed in a homogeneous way. The dolomitic matrix appears to be  
 438 dissolving superficially, with lighter shade silicate and sulfide grains highlighted (Fig. 13 SEM  
 439 P1-POST). The relative increase of iron, sulfur and silicon occurs, as well as the appearance of  
 440 chlorine and sodium of the brine (Fig. 13 EDX POST).

441 The existing sealed fissure in the axial and longitudinal CT image (Fig. 13 CT PRE) is not aligned  
 442 with the direction of the injection flow, indicating that the fluid has moved through the matrix

443 dissolving the minerals that they surround it (Fig. 13 CT POST, red arrows). The continuous  
 444 decrease in injection pressure from the initial 15 bar to the production of brine and CO<sub>2</sub>  
 445 collected in the separator (09) and gasometer (10) respectively, indicates once again that after  
 446 dissolution, there has been no entrainment of solids that collapse the flow advance (inlet-  
 447 outlet) towards the production line (Fig. 7).



448

449

450 **Fig. 13.** SEM, EDX and CT sample A6 previous (PRE) and subsequent (POST) to the injection.

451 The chemical processes are fully dependent on the amount of CO<sub>2</sub> dissolved in water (André et  
 452 al., 2007) and the composition of the brine (Crockford et al., 2014). The aqueous form of CO<sub>2</sub>,  
 453 not the molecular one, is reactive with the storage rock. The solubility of CO<sub>2</sub> is fully  
 454 dependent on pressure and on temperature and the ionic strength. Solubility is higher at  
 455 higher temperature, lower salinity and higher pressure. In the absence of any reaction with the  
 456 rock of the aquifer, the dissolved CO<sub>2</sub> results in an acid solution of pH=3.4 due to dissociation  
 457 of carbonic acid (Rosenbauer et al., 2005). The dissociation of carbonic acid to hydrogen ion

458 (reactive) and bicarbonate  $2\text{HCO}_3^- + \text{Ca}^{2+}$  initiates a series of complex reactions with the fluids  
459 present in the aquifer and rocks to fix  $\text{CO}_2$  in the aqueous and mineral phases. The fast  
460 dissolution of carbonates is the response to the decrease in pH (Ketzer et al., 2009).

461 After the injection carried out in the samples A5 and A6, a pH of 4 and 2 was measured in the  
462 production of fluids respectively.

463 When  $\text{CO}_2$  is injected into saline aquifer, basically, two types of reactions can occur, those that  
464 change the acidity of the formation and those that do not. The ratios of these reactions can  
465 vary from formation to formation and at different levels depending on the mineralogy and  
466 compositions of the fluids in the aquifer (De Silva et al., 2015). Generally, during the  $\text{CO}_2$   
467 injection in saline aquifers, its pH can vary from 3 to 7 close or far away from the injection well,  
468 respectively.

#### 469 **4. Discussion**

470 In hydraulic fracturing for the exploitation of hydrocarbon resources, large quantities of fluid  
471 are injected under pressure to create and propagate the fractures (Carpenter, N. F., 1962).  
472 With fractured acidizing, channels are created in the walls of existing fractures in the rock,  
473 which must be partially soluble in the acid used, limiting its application to generally carbonate  
474 reservoirs. Acidification according to the usual technique is usually better in shallow, low-  
475 temperature reservoirs (less than  $90^\circ\text{C}$ ) and with a maximum effective stress on fractures of  
476 less than 340 bar (Williams and Nierode, 1972). This reduces the reaction rate of the acid with  
477 the formation, allowing it to penetrate the fracture with greater depth before its effect is  
478 exhausted.

479 In ductile type limestone reservoirs, it is necessary to maintain a lower effective stress to  
480 achieve adequate conductivity in the fracture during the life of the wells. The reaction of the  
481 acid in a carbonate formation causes the release of fines, which occurs when the release  
482 torque generated by the hydrodynamic drag force exceeds the coupling torque generated by  
483 the electrostatic attraction force (Russell et al., 2018). When the flow velocities are higher, a  
484 greater drag force is produced and, therefore, an increase in the extent of the detachment of  
485 the particles (Zheng et al., 2014). On the other hand, the electrostatic force decreases when  
486 the fluid salinity is lower (Khilar et al., 1983; Shen et al., 2018), or with an increase in pH (Patil  
487 et al., 2011), resulting in a higher detachment of particles.

488 Aquifers with reduced primary or matrix porosity have drawbacks for  $\text{CO}_2$  storage, being  
489 necessary to act on them to improve their injectivity. Several studies indicate that the effects  
490 of injection of  $\text{CO}_2$ -saturated brine increases matrix porosity in the short term with an intensity  
491 that differs depending on whether the  $\text{CO}_2$  is in a gaseous or supercritical state (Peysson et al.,  
492 2014). Injection of  $\text{CO}_2$ -saturated brine results in a low pH that can cause dissolution of mineral  
493 cement and generation of particles with migration of fines (Othman et al., 2018b)

494 Mathematically it has been shown (Huang et al., 2018) that wettability influences the  
495 interfacial forces acting on fine particles, with their subsequent associated displacement.  
496 Capillary forces or wettability can reduce injection when fine migration occurs (Guo et al.,  
497 2018; Checker et al., 2018; Russell et al., 2018), with pore blockage during  $\text{CO}_2$  sequestration  
498 tests (Othman et al., 2018a).

499 During the acidification process with acid mixtures in a naturally fractured carbonate aquifer,  
500 the migration of fines causes an increase in the pressure drawdown and a decrease in the  
501 injection ratio.

502 From the first stages of injection into the well, a movement of particles occurs that affects  
503 predictions based on laboratory tests, where the injection rate obtained can be less than half  
504 of the initial value (Russell et al., 2018).

505 The use of HCl and Acetic acids favors the increase of the secondary porosity of the storage,  
506 where a higher concentration of HCl causes an increase in the dissolution of the carbonates  
507 that causes a greater drag of fines and the consequent blockage of the injection, reflected in  
508 the increase in both injection pressure and incremental pressure. The injection of 10% HCl  
509 produces the dissolution of the carbonate matrix (Fig. 8), compared to 15% where a  
510 dissolution of the carbonates near the fissures occurs (Fig. 9 & 10). In the case of open fissures,  
511 the surface free attack produces the appearance of cavities in these areas (Fig. 10), with less  
512 dissolution produced when they are filled (Fig. 9). On the other hand, the injection of the  
513 HCl/Acetic mixture with a concentration of 10%/10% generates a greater range and less  
514 production of cavities as a consequence of the greater dissolution of the matrix (Fig. 11).  
515 However, the greater phenomena of dissolution and entrainment of solids cause continuous  
516 production blockages, with high injection pressures, which do not allow stabilization (Fig. 6).

517 The scCO<sub>2</sub> injection appears to be weakly reactive, with limited modification of well injectivity.  
518 The CO<sub>2</sub> reacts firstly dissolving in the aqueous solution with an increase in the acidity of the  
519 brine and the potential mineral dissolution, favoring the increase of the porosity. The injection  
520 of brine saturated with CO<sub>2</sub> (Picot-Colbeaux et al., 2009, Farquahar et al., 2015, Pokrovsky et  
521 al., 2005) causes the dissolution of calcite, dolomite and anhydrite, with an increase of both  
522 the porosity and the permeability and a decrease in the pH of the effluents. The dissolution  
523 ratio of the calcite in the rocks depends on the amount of CO<sub>2</sub>/brine mixture, the local  
524 permeability, which allows the passage and distribution of the acidic brine, and the  
525 accessibility to the mineral (Lammy-Chappuis et al., 2013).

526 The previous results of tests in which we have participated indicated the effect on the porosity  
527 of the storage in fractured carbonates when scCO<sub>2</sub> was injected with or without impurities. In  
528 samples with primary porosity (18.87%), the injection of scCO<sub>2</sub> produces an increase in such  
529 porosity (21.02%). On the other hand, when the injection contains impurities the mixture is  
530 not in a supercritical state, at P and T conditions of pure scCO<sub>2</sub>, which produces a decrease of  
531 the primary porosity from 8.94% to 1.95% (de Dios et al., 2016).

532 Injecting the pure scCO<sub>2</sub> mixture with brine requires lower injection pressures and there are no  
533 blockages in the incremental pressure (Fig. 7). The production of brine in the separator and  
534 CO<sub>2</sub> in the gasometer ensure a dissolution of the matrix and the consequent increase in  
535 secondary porosity without a massive dissolution of the carbonates and fines entrainment (Fig.  
536 13 & 14). The tests of this work carried out the injection of pure scCO<sub>2</sub> and brine verifying the  
537 production of fluids, and assuming a migration dominated by the existence of fractures (de  
538 Dios et al., 2017). In these areas the injection process involved the dissolution of the  
539 carbonates that surrounded the aluminosilicates, anhydrite, quartz and iron sulfides that  
540 sealed the fractures, with a slight drag of fines.

## 541 **5. Conclusions**

542 The methodology for the injection of acid mixtures in the ATAP experimental facility, together  
543 with the macroscopic observation by means of imaging techniques of the injection surface and  
544 the interior of the samples, makes it possible to study a formation for CO<sub>2</sub> storage.

545 Naturally fractured carbonate formations with low porosity and permeability are hardly  
546 susceptible to constituting a CO<sub>2</sub> store due to their low injectivity and capacity associated.  
547 Injection of acidic mixtures with different proportions of HCl, Acetic and scCO<sub>2</sub>/brine has  
548 effects on injection pressures, pressure drop and the production of the corresponding fluids.

549 **5.1. Acid injection (HCl, Acetic)**

1 550 The injection of HCl and Acetic mixtures in different proportions entails a dissolution of the  
2 551 mineral matrix, resulting to be greater with higher concentrations of HCl (15%).

3  
4 552 The solution is generally associated with a displacement of the particles present in the filling of  
5 553 the fissures, consisting in this case of potassium aluminosilicates, anhydrite, quartz and iron  
6 554 sulphides that cause blockages and interconnections of the pores. This fact is confirmed in the  
7 555 injection pressure values obtained during the tests with HCl and Acetic and with the non-  
8 556 monotonic incremental pressure values, which implies a reduction in the permeability of the  
9 557 samples, and therefore, the aquifer injectivity under these injection conditions.

10  
11  
12 558 Injecting acidic HCl and Acetic mixtures that are not part of the underground CO<sub>2</sub> storage  
13 559 system is an artificial technique to increase secondary porosity, injectivity, and storage  
14 560 capacity. The increase in secondary porosity produced by dissolution of the rocky matrix and  
15 561 entrainment of fines can generate preferential paths of CO<sub>2</sub> diffusion towards the seal. In  
16 562 addition, the high pressures generated and the opening of enlarged fractures will cause a lack  
17 563 of sealing, making storage not safe in the long term.

18  
19  
20 564 On the other hand, the increase in injection pressure due to the collapse of the pores  
21 565 produced by the entrained fines can compromise its tightness in the short term by exceeding  
22 566 the fracture pressure.

23  
24 567 **5.2. scCO<sub>2</sub> enriched brine injection**

25 568 The injection of the scCO<sub>2</sub>/brine mixture, although produces also the dissolution of the mineral  
26 569 matrix, this is not so high, resulting in a lower drag of fines for the same injection flow rate  
27 570 than in the case of HCl and Acetic injection.

28  
29 571 The injection and incremental pressures obtained during the movement of the scCO<sub>2</sub>/brine  
30 572 mixture through the sample have been lower and decreasing since the start of the injection.  
31 573 From the start, CO<sub>2</sub> production has been observed in the gasometer and brine production in  
32 574 the separator with negligible pore blockage, which represents an improvement in the  
33 575 injectivity of the samples and an increase in secondary porosity. The dissolution of the matrix  
34 576 occurs without the opening of enlarged fissures/fractures that could compromise the safety of  
35 577 the storage.

36  
37  
38 578 The process to increase storage injectivity with the scCO<sub>2</sub>/brine mixture, which occurs  
39 579 naturally by injecting scCO<sub>2</sub> into the aquifer, would be associated with the storage process. The  
40 580 increase in secondary porosity caused by the injection of scCO<sub>2</sub>/brine improves the injectivity  
41 581 and capacity of the storage, presenting itself as an economically and technically profitable  
42 582 alternative for the susceptible aquifers to store CO<sub>2</sub>. The use of scCO<sub>2</sub> enriched brine against  
43 583 the injection of acids to improve the injectivity, supposes a safe operation of storage of CO<sub>2</sub> by  
44 584 the phenomenon of controlled dissolution-precipitation of carbonates, which favors the trap  
45 585 mechanisms of solubility trapping and mineral trapping, ensuring the tightness of the storage.

46  
47  
48 586 For a better knowledge of the entrainment phenomenon, the analysis of the concentration of  
49 587 fines in the acidic mixtures or in the brine produced is proposed, as well as a control of the pH  
50 588 variations associated with the chemical reactions developed in the samples.

51  
52 589 **Acknowledgements**

53  
54 590 We thank the CIUDEN (Fundación Ciudad de la Energía) for providing us with the samples used  
55 591 in this work from the Hontomín PDT (European Energy Programme for Recovery).

56  
57 592 **References**

- 593 Abba M.A., Abbas A.J., Nasr G.G., Al-Otaibi A., Burby M., Saidu B., Suleiman S.M. 2019.  
594 Solubility trapping as a potential secondary mechanism for CO<sub>2</sub> sequestration during  
595 enhanced gas recovery by CO<sub>2</sub> injection in conventional natural gas reservoirs: An  
596 experimental approach. *Journal of Natural Gas Science and Engineering*, 71, 103002.  
597 <https://doi.org/10.1016/j.jngse.2019.103002>
- 598 Agnaou, M., Lasseux, D., Ahmadi, A. 2017 Origin of the inertial deviation from Darcy's law: An  
599 investigation from a microscopic flow analysis on two-dimensional model structures. *Physical*  
600 *Review E*. <https://doi.org/10.1103/PhysRevE.96.043105>
- 601 Al-Awad, M. N. J., 2001. Relationship between reservoir productivity and pore pressure drop.  
602 *Journal of King Saud university- Engineering Sciences*. Vol 13 (1), 137-150.  
603 [https://doi.org/10.1016/S1018-3639\(18\)30730-X](https://doi.org/10.1016/S1018-3639(18)30730-X)
- 604 Al-Khulaifia, Y., Lina, Q., Blunta, M. J., Bijeljica, B. 2018. Reservoir-condition pore-scale imaging of  
605 dolomite reaction with supercritical CO<sub>2</sub> acidified brine: Effect of pore-structure on reaction rate  
606 using velocity distribution analysis. *Int. J. Greenh. Gas Control* 68, 99-111.  
607 <https://doi.org/10.1016/j.ijggc.2017.11.011>
- 608 American Petroleum Institute (API). Acidizing treatment in oil and Gas Operators, 2014.  
609 Briefing Paper. Digital Media | DM2014-113 | 05.14 | PDF.
- 610 André, L., Audigane, P., Azaroual, M., Menjuz, A., 2007. Numerical modeling of fluid-rock chemical  
611 interactions at the supercritical CO<sub>2</sub>-liquid interface during CO<sub>2</sub> injection into a carbonate  
612 reservoir, the Dogger aquifer (Paris Basin, France). *Energy Convers. Manage.* 48 (6), 1782-1797.  
613 <https://doi.org/10.1016/j.enconman.2007.01.006>
- 614 Barkman, J., Abrams, A., Darley, H., Hill, H., 1975. An oil-coating process to stabilize clays in  
615 fresh waterflooding operations (includes associated paper 6405). *J. Petrol. Technol.* 27 (09),  
616 1053-1059. <https://doi.org/10.2118/4786-PA>
- 617 Byrne, M.T., Waggoner, S.M., 2009. Fines migration in a high temperature gas reservoir -  
618 laboratory simulation and implications for completion design. In: SPE-121897. SPE European  
619 Formation Damage Conference Held in Scheveningen, the Netherland, 27-29 May.  
620 <https://doi.org/10.2118/121897-MS>
- 621 Carpenter, N. F. 1962. United States Patent Office. 3252904: Acidizing and Hydraulic fracturing  
622 of wells. The Dow Chemical Company, Midland. July 9. Ser. No. 208252.
- 623 Civan, F., 2007. *Reservoir Formation Damage: Fundamentals, Modeling, Assessment, and*  
624 *Mitigation*. Gulf Professional Publishing, Elsevier, Burlington, USA.
- 625 Crockford, P., Telmer, K., Best, M., 2014. Dissolution kinetics of Devonian carbonates at  
626 circum-neutral pH, 50 bar *p*CO<sub>2</sub>, 105°C and 0.4 M: The importance of complex brine chemistry  
627 on reaction rates. *Applied Geochemistry* 41, 128-134.  
628 <https://doi.org/10.1016/j.apgeochem.2013.12.008>
- 629 Chen, D., Pan, Z., Ye, Z., 2015a. Dependence of gas shale fracture permeability on effective  
630 stress and reservoir pressure: model match and insights. *Fuel* 139, 383-392.
- 631 Chen, Y.F., Hu, S.H., Hu, R., Zhou, C.B., 2015b. Estimating hydraulic conductivity of fractured  
632 rocks from high-pressure packer tests with an Izbash's law based empirical model. *Water*  
633 *Resour. Res.* 51 (4), 2096e2118. <https://doi.org/10.1002/2014WR016458>
- 634 Chequer, L., Vaz, A., Bedrikovetsky, P., 2018. Injectivity decline during low-salinity  
635 waterflooding due to fines migration. *J. Pet. Sci. Eng.* 165, 1054-1072.  
636 <https://doi.org/10.1016/j.petrol.2018.01.012>

- 637 Dawson, G., Pearce, J., Biddle, D., Golding, S., 2015. Experimental mineral dissolution in Berea  
638 Sandstone reacted with CO<sub>2</sub> or SO<sub>2</sub>-CO<sub>2</sub> in NaCl brine under CO<sub>2</sub> sequestration conditions.  
639 Chem. Geol. 399, 87-97. <https://doi.org/10.1016/j.chemgeo.2014.10.005>
- 640 de Dios, J.C., Delgado, M.A., Marín, J.A., Martínez, C., Ramos, A., Salvador, I., Valle, L., 2016.  
641 Short-term effects of impurities in the CO<sub>2</sub> stream injected into fractured carbonates. Int. J.  
642 Greenh. Gas Control 54 (2), 727-736. <https://doi.org/10.1016/j.ijggc.2016.08.032>
- 643 de Dios, J.C., Delgado, M.A., Martínez, C., Ramos, A., Álvarez, I., Marín, J.A., Salvador, I., 2017.  
644 Hydraulic characterization of fractured carbonates for CO<sub>2</sub>geological storage: Experiences and  
645 lessons learned in Hontomín Technology Development Plant. Int. J. Greenh. Gas Control 58, 185-  
646 200. <https://doi.org/10.1016/j.ijggc.2017.01.008>
- 647 de Dios, J.C., Le gallo, Y., Marín, J.A., 2018. Innovative CO<sub>2</sub> injections in carbonates and advanced  
648 modelling for numerical investigation. Preprints 2018.  
649 <https://doi.org/10.20944/preprints201807.0537.v1>
- 650 de Silva, G.P.D., Ranjith, P.G., Perea, M.S.A., 2015. Geochemical aspects of CO<sub>2</sub> sequestration in  
651 deep saline aquifer: A review. Fuel 155, 128-143. <https://doi.org/10.1016/j.fuel.2015.03.045>
- 652 Farajzadeh, R., Lotfollahi, M., Lake, L.W., 2016. Simultaneous sorption and mechanical  
653 entrapment during polymer flow through porous media. Water Resour. Res. 52 (3), 2279-2298.  
654 <https://doi.org/10.1002/2015WR017885>
- 655 Farquhar, S.M., Pearce, J.K., Dawson, G.K.W., Golab, A. Sommacal, S., D. Kirste, D., Biddle, D.,  
656 Golding, S. M., 2015. A fresh approach to investigating CO<sub>2</sub> storage: Experimental CO<sub>2</sub>-water-  
657 rock interactions in a low-salinity reservoir system. Chemical Geology 399, 98-122.  
658 <https://doi.org/10.1016/j.chemgeo.2014.10.006>
- 659 Folomeev, A. E., Sharifullin, A.R., Vakhrushev, S.A., Murinov, K.Yu., Akimkin, A.V.,  
660 Lenchenkova, L.E., Nabiullin, R.M., Federov, A.I. 2014. Theory and Practice of Acidizing High  
661 Temperature Carbonate Reservoirs of R. Trebs Oil Field, Timan-Pechora Basin. SPE-171242-MS.  
662 SPE Russian Oil and Gas Exploration & Production Technical Conference and Exhibition, 14-16  
663 October, Moscow, Russia. <https://doi.org/10.2118/171242-MS>.
- 664 Guo, Z., Vu, P.N.H., Hussain, F., 2018. A laboratory study of the effect of creep and fines  
665 migration on coal permeability during single-phase flow. Int. J. Coal Geol. 200, 61-76.  
666 <https://doi.org/10.1016/j.coal.2018.10.009>
- 667 Holzheid, A., 2016. Dissolution kinetics of selected natural minerals relevant to potential CO<sub>2</sub>-  
668 injection sites- Part 1: A review. Geochemistry 76, 621-641.  
669 <https://doi.org/10.1016/j.chemer.2016.09.007>
- 670 Holzheid, A., 2016. Dissolution kinetics of selected natural minerals relevant to potential CO<sub>2</sub>-  
671 injection sites- Part 2: Dissolution and alteration of carbonates and feldspars in CO<sub>2</sub>-bearing  
672 brines. Geochemistry 76, 643-657. <https://doi.org/10.1016/j.chemer.2016.09.008>
- 673 Hong, Y. , Fei, L., Heng, X., Yu, S., Changlin, Z., Yezhong, W. 2018. Numerical simulation and field  
674 application of diverting acid acidizing in the lower Cambrian Longwangmiao Fm gas reservoirs  
675 in the Sichuan Basin. Natural Gas Industry B (5), 3, 204-211.  
676 <https://doi.org/10.1016/j.ngib.2018.04.007>
- 677 Huang, F., Kang, Y., You, L., Li, X., You, Z., 2018. Massive fines detachment induced by moving  
678 gas-water interfaces during early stage two-phase flow in coalbed methane reservoirs. Fuel  
679 222, 193-206. <https://doi.org/10.1016/j.fuel.2018.02.142>
- 680 Hurtado Bezos, A., 2012. Estimación de la capacidad de almacenamiento geológico de CO<sub>2</sub>.

- 681 Metodología e incertidumbres. Editorial Académica Española, 452 pages. ISBN-13: 978-  
682 3847355922.
- 683 Iding, M., Ringrose, P., 2010. Evaluating the impact of fractures on the performance of the In Salah  
684 CO2 storage site. *Int. J. Greenh. Gas Control* 4, 242-248.  
685 <https://doi.org/10.1016/j.ijggc.2009.10.016>
- 686 Jean, J.S., Wang, C.L., Hsiang, H.I., Li, Z., Yang, H.J., Jiang, W.T., Yang, K.M., Bundschuh, J., 2015.  
687 Experimental investigation of trace element dissolution in formation water in the presence of  
688 supercritical CO2 fluid for a potential geological storage site of CO2 in Taiwan. *J. Nat. Gas Sci.*  
689 *Eng.* 23, 304-314. <https://doi.org/10.1016/j.jngse.2015.02.006>
- 690 Kampman, N., Bickle, M., Wigley, M. Dubacq, B., 2014. Fluid flow and CO2-fluid-mineral  
691 interactions during CO2-storage in sedimentary basins. *Chemical Geology* 369, 22-50.  
692 <https://doi.org/10.1016/j.chemgeo.2013.11.012>
- 693 Ketzer J, Iglesias R, Einloft S, Dullius J, Ligabue R, De Lima V. Water-rock-CO2 interactions in  
694 saline aquifers aimed for carbon dioxide storage: experimental and numerical modeling studies  
695 of the Rio Bonito Formation (Permian), southern Brazil. *Appl Geochem* 2009; 24:760-7.  
696 <https://doi.org/10.1016/j.apgeochem.2009.01.001>
- 697 Khilar, K.C., Fogler, H.S., Ahluwalia, J., 1983. Sandstone water sensitivity: existence of a critical  
698 rate of salinity decrease for particle capture. *Chem. Eng. Sci.* 38 (5), 789-800.  
699 [https://doi.org/10.1016/0009-2509\(83\)80188-2](https://doi.org/10.1016/0009-2509(83)80188-2)
- 700 Khilar, K.C., Fogler, H.S., 1998. *Migration of Fines in Porous Media*. Kluwer Academic  
701 Publishers, Dordrecht.
- 702 Kovács, T., 2014. Characterization of the Hontomin reservoir and seal formations. *Proceedings*  
703 *of the 4th Spanish-French Symposium on CO2 Geological storage*.
- 704 Lamy-Chappuis, B., Angus, D., Fisher, Q., Grattoni C., Yardley, B.W.D., 2013. Rapid porosity and  
705 permeability changes of calcareous sandstone due to CO2-enriches brine injection. *Agu*  
706 *Publications. Geophysical Research Letters.* 10.1002/2013GL058534. *Res. Lett.* 41,399-406.  
707 <https://doi.org/10.1002/2013GL058534>
- 708 Landau, L., Lifshitz, E. 1987. *Fluid Mechanics. Vol 6. Course of theoretical Physics*.
- 709 Le Gallo, Y., De Dios, J.C., 2018. Geological Model of a storage Complex for a CO2 storage  
710 Operation in a Naturally-Fractured Carbonate Formation. *Geosciences* 8, 354.  
711 <https://doi.org/10.3390/geosciences8090354>
- 712 Lenormand R., Touboul E., Zarcone C. 1988. Numerical models and experiments on immiscible  
713 displacements in porous media. *Journal of Fluid Mechanics*, 189, 165-187.  
714 <https://doi.org/10.1017/S0022112088000953>
- 715 Lenormand R. CydarR. Cydarex, 2012.
- 716 Li, N., Dai, J., Liu, Ch., Liu, P., Zhang, Y., Luo, Z. 2015. Feasibility study on application of volume  
717 acid fracturing technology to tight gas carbonate reservoir development. *Petroleum* 1, 206-  
718 216. <https://doi.org/10.1016/j.petlm.2015.06.002>
- 719 Liqiang, Z., Yiyong, P., Yigang, L., Xianghai, M., Yujie, G., Pingli, L. 2018. Research and  
720 performance evaluation on an HA integrated acid system for sandstone acidizing. *Natural Gas*  
721 *Industry B* (5), 2, 156-161. <https://doi.org/10.1016/j.ngib.2018.04.002>
- 722 Middleton R. S., Carey, J. W., Currier, R.P., Hyman, J.D., Kang, Q., Karra, S., Jiménez-Martínez,  
723 J., Porter M. L., Viswanathan, H. S. 2015. Shale gas and non-aqueous fracturing fluids:

724 Opportunities and challenges for supercritical CO<sub>2</sub>. *Applied Energy*, 147, 500-509.  
725 <https://doi.org/10.1016/j.apenergy.2015.03.023>

726 Mitiku, A.B., Bauer, D.L.S., Beyer, C., 2013. Geochemical modeling of CO<sub>2</sub>-water-rock interactions  
727 in a potential storage formations of the North German sedimentary basin. *Applied Geometry* 36,  
728 68-186. <https://doi.org/10.1016/j.apgeochem.2013.06.008>

729 Nazridoust, K., Ahmadi, G., Smith, D.H. 2006. A new friction factor correlation for laminar,  
730 single-phase flows through rock fractures. *Journal Hydrogeology* 329, 315-328.  
731 <https://doi.org/10.1016/j.jhydrol.2006.02.032>

732 Othman, F., Wang, Y. & Hussain, F. 2018a. The Effect of Fines Migration During CO<sub>2</sub> Injection  
733 Using Pore Scale Characterization. SPE Asia Pacific Oil and Gas Conference and Exhibition.  
734 Brisbane, Australia: Society of Petroleum Engineers. <https://doi.org/10.2118/192076-MS>

735 Othman, F., Yu, M., Kamali, F. & Hussain, F. 2018b. Fines migration during supercritical CO<sub>2</sub>  
736 injection in sandstone. *Journal of Natural Gas Science and Engineering*, 56, 344-357.  
737 <https://doi.org/10.1016/j.jngse.2018.06.001>

738 Patil, S., Tawfiq, K., Chen, G., 2011. Colloid release and transport in agricultural soil as  
739 impacted by solution chemistry. *J. Urban Environ. Eng.* 5 (2), 84-90.  
740 <https://doi.org/10.4090/juee.2011.v5n2.084090>

741 Peysson, Y., André, L., Azaroual, M., 2014. Well injectivity during CO<sub>2</sub> storage operations in deep  
742 saline aquifers- Part 1: Experimental investigation of drying effects, salt precipitation and capillary  
743 forces. *Int. J. Greenh. Gas Control* 22, 291-300. <https://doi.org/10.1016/j.ijggc.2013.10.031>

744 Phuc Vu, H., Black, .R, Haese, R.R., 2018. The geochemical effects of O<sub>2</sub> and SO<sub>2</sub> as CO<sub>2</sub>  
745 impurities on fluid-rock reactions in a CO<sub>2</sub> storage reservoir. *Int. J. Greenh. Gas Control* 68, 86-  
746 98. <https://doi.org/10.1016/j.ijggc.2017.11.001>

747 Picot-Colbeaux, G., Pettenati, M., Thiéry, D., Kervévan, Ch., André, L., Azaroual, M., 2009.  
748 Numerical modeling of fluid-rock chemical interactions during CO<sub>2</sub> saturated water injection into  
749 sandstone reservoir, using the MARTHE-REACT code. Proceedings TOUGH Symposium, Lawrence  
750 Berkeley National Laboratory, Berkeley, California, September 14-16.  
751 <https://hal-brgm.archives-ouvertes.fr/hal-01073955>

752 Pokrovsky, O. S., Golubev, S.V., Schott, J., 2005. Dissolution kinetics of calcite, dolomite and  
753 magnesite at 25°C and 0 to 50 atm pCO<sub>2</sub>, *Chem. Geol.* 217 (3-4), 239-255.  
754 <https://doi.org/10.1016/j.chemgeo.2004.12.012>

755 Portier, S., André, L., Vuataz, F-D. 2007. Review on chemical stimulation techniques in oil  
756 Industry and applications to geothermal systems. Technical Report. CREGE - Centre for  
757 Geothermal Research, Neuchâtel, Switzerland.

758 Prommer, H., et al., 2013. Final Report - Aquifer Storage and Recovery of Potable Water in the  
759 Leederville Aquifer. CSIRO Water for a Healthy Country National Research Flagship, Australia.

760 Pudlo, D., Henkel, S., Reitenbach, V., Albrecht, D., Enzmann, F., Heister, K., Pronk, G., Ganzer,  
761 L., Gaupp, R., 2015. The chemical dissolution and physical migration of minerals induced during  
762 CO<sub>2</sub> laboratory experiments: their relevance for reservoir quality. *Environ. Earth Sci.* 73, 7029-  
763 7042. <https://doi.org/10.1007/s12665-015-4411-x>

764 Richeng L., Liyuan Y., Yujing J. 2016. Fractal analysis of directional permeability of gas shale  
765 fracture networks: A numerical study. *Journal of Natural Gas Science and Engineering* 33,  
766 1330-1341. <https://doi.org/10.1016/j.jngse.2016.05.043>

- 767 Rosenbauer, R. J., Koksalan, T., Palandri, L., 2005. Experimental investigation of CO<sub>2</sub>-brine-rock  
768 interactions at elevated temperature and pressure: Implications for CO<sub>2</sub> sequestration in  
769 deep-saline aquifers, Fuel Process. Technol. 86 (14-15), 1581-1597.  
770 <https://doi.org/10.1016/j.furpoc.2005.01.011>
- 771 Rubio, F.M., García, J., Ayala, C., Rey, C., García Lobón, J.L., 2014. Gravimetric characterization  
772 of the geological structure of Hontomin. 8ª Asamblea Hispano-Lusa de Geodesia y Geofísica,  
773 Évora (Portugal), 29-31 January 2014.
- 774 Russell, T., Pham, D., Neishaboor, M.T., Badalyan, A., Behr, A., Genolet, L., Kowollik, P.,  
775 Zeinijahromi, A., Bedrikovetsky, P. 2017. Effects of Kaolinite in rocks on fines migration. Journal  
776 of natural Gas Science and Engineering 45, 243-255.  
777 <https://doi.org/10.1016/j.jngse.2017.05.020>
- 778 Russell, T., Wong, K., Zeinijahromi, A., Bedrikovetsky, P. 2018. Effects of delayed particle  
779 detachment on injectivity decline due to fines migration. Journal of Hydrology 564, 1099-1109.  
780 <https://doi.org/10.1016/j.jhydrol.2018.07.067>
- 781 Sayegh, S., Krause, F., Girard, M., Debree, C., 1990. Rock/fluid interactions of carbonated  
782 brines in a sandstone reservoir: pembina Cardium, Alberta, Canada. SPE Form. Eval. 5, 399-  
783 405.  
784 <https://doi.org/10.2118/19392-PA>
- 785 Schön, J. H., 2015. Physical Properties of Rocks. Fundamentals and Principles of Petrophysics.  
786 Vol 65, 2-497, 2<sup>nd</sup> edition. Elsevier B.V. ISBN: 978-0-08-100404-3; ISSN: 0376-7361.
- 787 Shen, C., Bradford, S.A., Li, T., Li, B., Huang, Y., 2018. Can nanoscale surface charge  
788 heterogeneity really explain colloid detachment from primary minima upon reduction of  
789 solution ionic strength? J. Nanopart Res. 20 (6).  
790 <https://doi.org/10.1007/s11051-018-4265-8>
- 791 Soong, Y., Goodman, A.L., McCathy-Jones, J.R., 2004. Experimental and simulation studies on  
792 mineral trapping of CO<sub>2</sub> with brine. Energy Conversion Management 45, 1845-1859.  
793 <https://doi.org/10.1016/j.enconman.2003.09.029>
- 794 Soulaire, C. On the origin of Darcy's Law. Chapter 1. 2015.  
795 [https://web.stanford.edu/~csoulain/PORE\\_SCALE/Chap1\\_Darcy.pdf](https://web.stanford.edu/~csoulain/PORE_SCALE/Chap1_Darcy.pdf) Csoulain@stanford.edu
- 796 Tongjun, M., Boming, Y., Yonggang, D., Quantang, F. 2015. A fractal analysis of permeability for  
797 fractured rocks. International Journal of heat and mass transfer.  
798 <https://doi.org/10.1016/j.ijheatmasstransfer.2014.10.010>
- 799 Valle, L.M., Martínez, C., 2015. Patente Nacional: Equipo para ensayos petrofísicos.  
800 P201231913.2015.
- 801 Valle L.M., Rodríguez R., Grima C., Martínez C., 2018. Effects of supercritical CO<sub>2</sub> injection on  
802 sandstone trapping wettability and capillary trapping. Int. J. Greenh. Gas Control 78, 341-348.  
803 <https://doi.org/10.1016/j.ijggc.2018.09.005>
- 804 Wang, F.P., Reed, R.M., 4e7 October 2009. Pore networks and fluid flow in gas shales. In: SPE  
805 Annual Technical Conference and Exhibition. New Orleans, Louisiana, USA.
- 806 Wang, Y., Crandall, D., Bruner K, Ning W., Gill, M., Xiaochun, L., Bromhal, G., 2013. Core and pore  
807 scale characterization of Liujiagou Outcrop sandstone, Ordos basin, China for CO<sub>2</sub> Aquifer  
808 Storage. Energy Procedia 37, 5055-5062. <https://doi.org/10.1016/j.egypro.2013.06.419>
- 809 Williams, B.B., Nierode, D. E. 1972. Design of acid fracturing treatments. SPE-3720-PA, 24, 07.

810 <https://doi.org/10.2118/3720-PA>

1  
2 811 Yan, Q., Lemanski, C., Karpyn, Z. T., Ayala, L. F. 2015. Experimental investigation of shale gas  
3 812 production impairment due to fracturing fluid migration during shut-in time. Journal of Natural  
4 813 Gas Science and Engineering, 24, 99-105. <https://doi.org/10.1016/j.jngse.2015.03.017>

5  
6 814 Yuan, B., Wood, D.A., Yu, W., 2015. Stimulation and hydraulic fracturing technology in natural  
7 815 gas reservoirs: theory and case studies (2012-2015). J. Nat. Gas Sci. Eng. 26, 1414-1421.  
8 816 <https://doi.org/10.1016/j.jngse.2015.09.001>

9  
10 817 Yunzhong, J., Yiyu, L., 2018. Surface characteristics and permeability enhancement of shale  
11 818 fractures due to water and supercritical carbon dioxide fracturing. Journal of petroleum  
12 819 science and Engineering. <https://doi.org/10.1016/j.petrol.2018.02.018>

13  
14 820 Zeinijahromi, A., Farajzadeh, R., Bruining, J., 2016. Effect of fines migration on Oil-water  
15 821 relative permeability during two-phase flow in porous media. Fuel 176, 222-236.  
16 822 <https://doi.org/10.1016/j.fuel.2016.02.066>

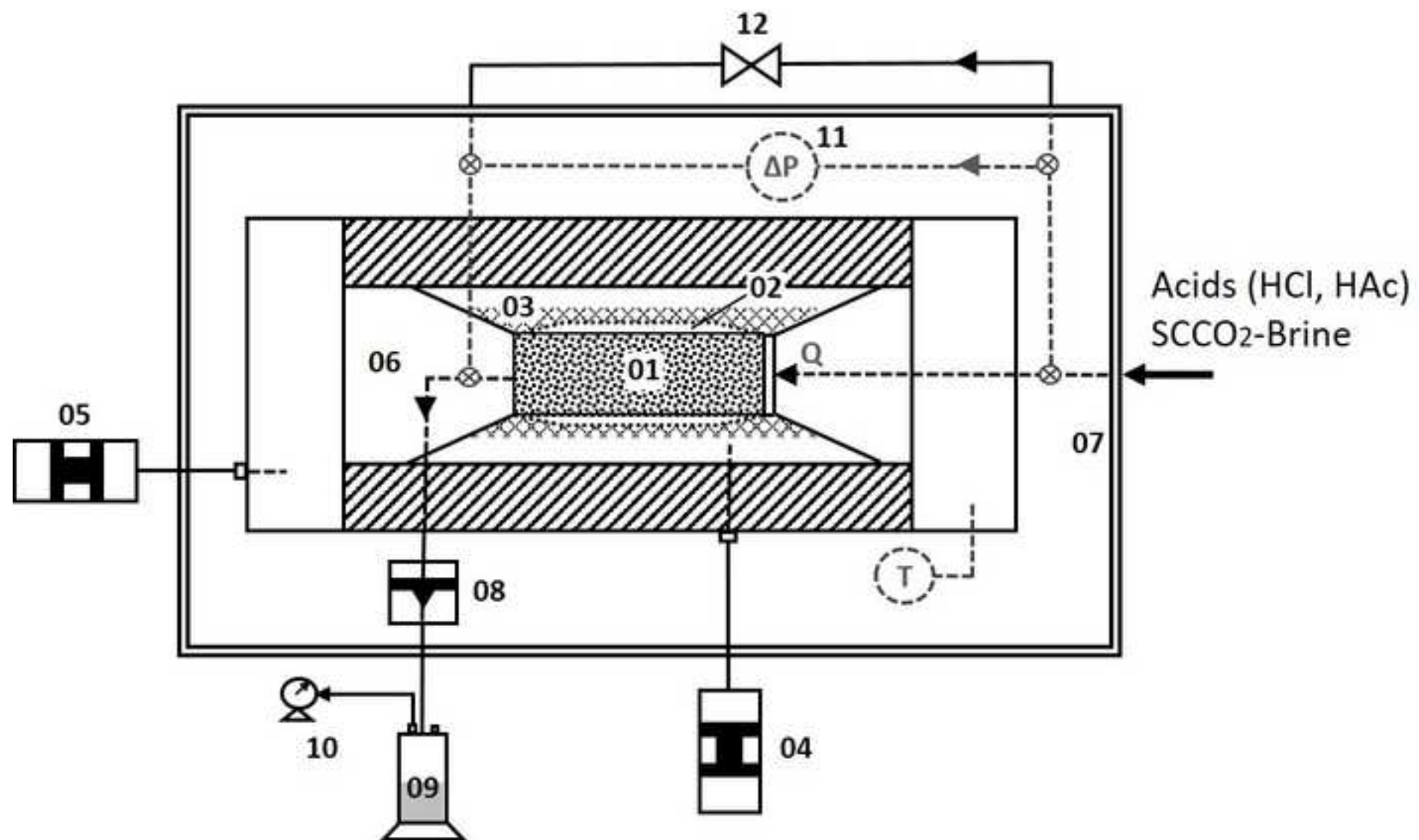
17  
18 823 Zhang, X., Ge, J., Kamali, F., Othman, F., Wang, Y., Le-Hussain, F. 2020. Wettability of sandstone  
19 824 rocks and their mineral components during CO2 injection in aquifers: Implications for fines  
20 825 migration. Journal of Natural gas Science and Engineering, 73, 103050.  
21 826 <https://doi.org/10.1016/j.jngse.2019.103050>

22  
23 827 Zhao, Z., Jing, L., Neretnieks, I., Moreno, L., 2011. Numerical modeling of stress effects on  
24 828 solute transport in fractured rocks. Comput. Geotech. 38 (2), 113-126.

25  
26 829 Zheng, X.L., Shan, B.B., Chen, L., Sun, Y.W., Zhang, S.H., 2014. Attachment-detachment  
27 830 dynamics of suspended particle in porous media: experiment and modeling. J. Hydrol. 511,  
28 831 199-204.  
29 832 <https://doi.org/10.1016/j.jhydrol.2014.01.039>

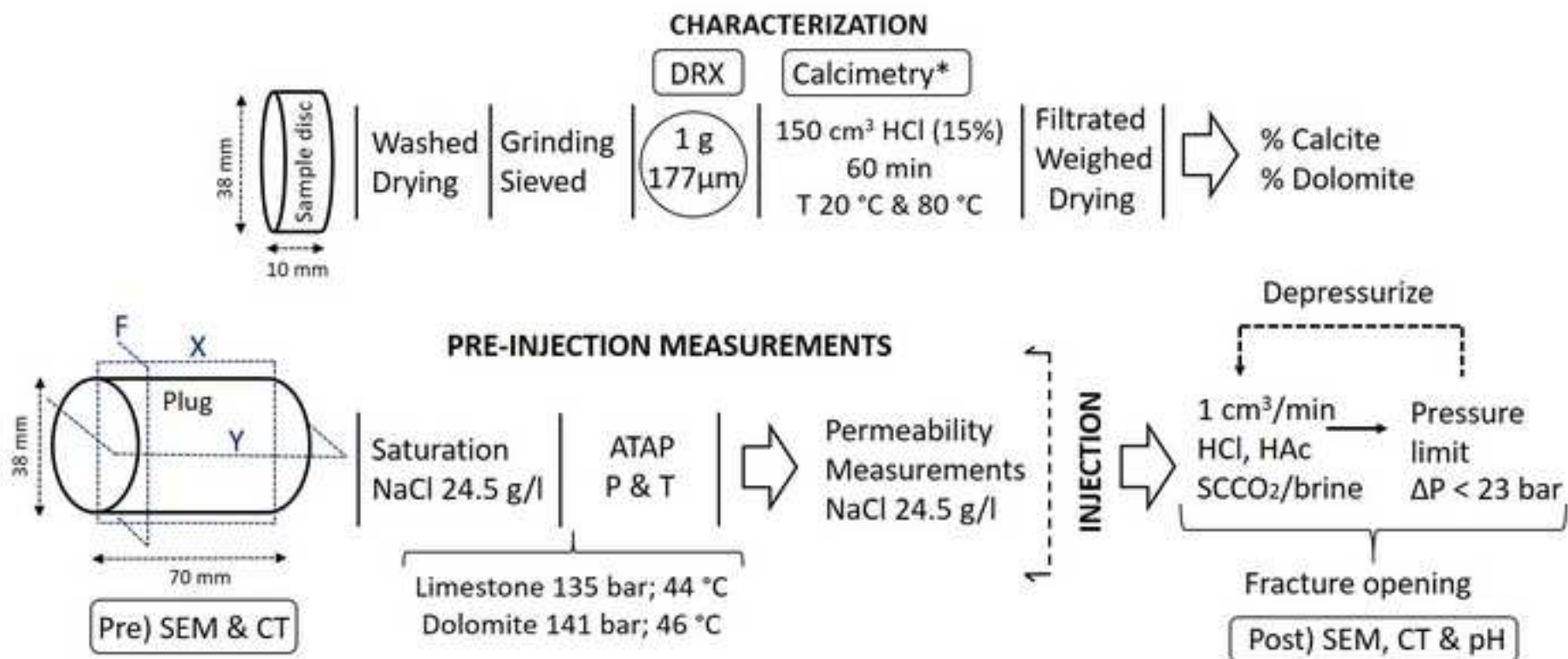
Figure

[Click here to download high resolution image](#)



Figure

[Click here to download high resolution image](#)

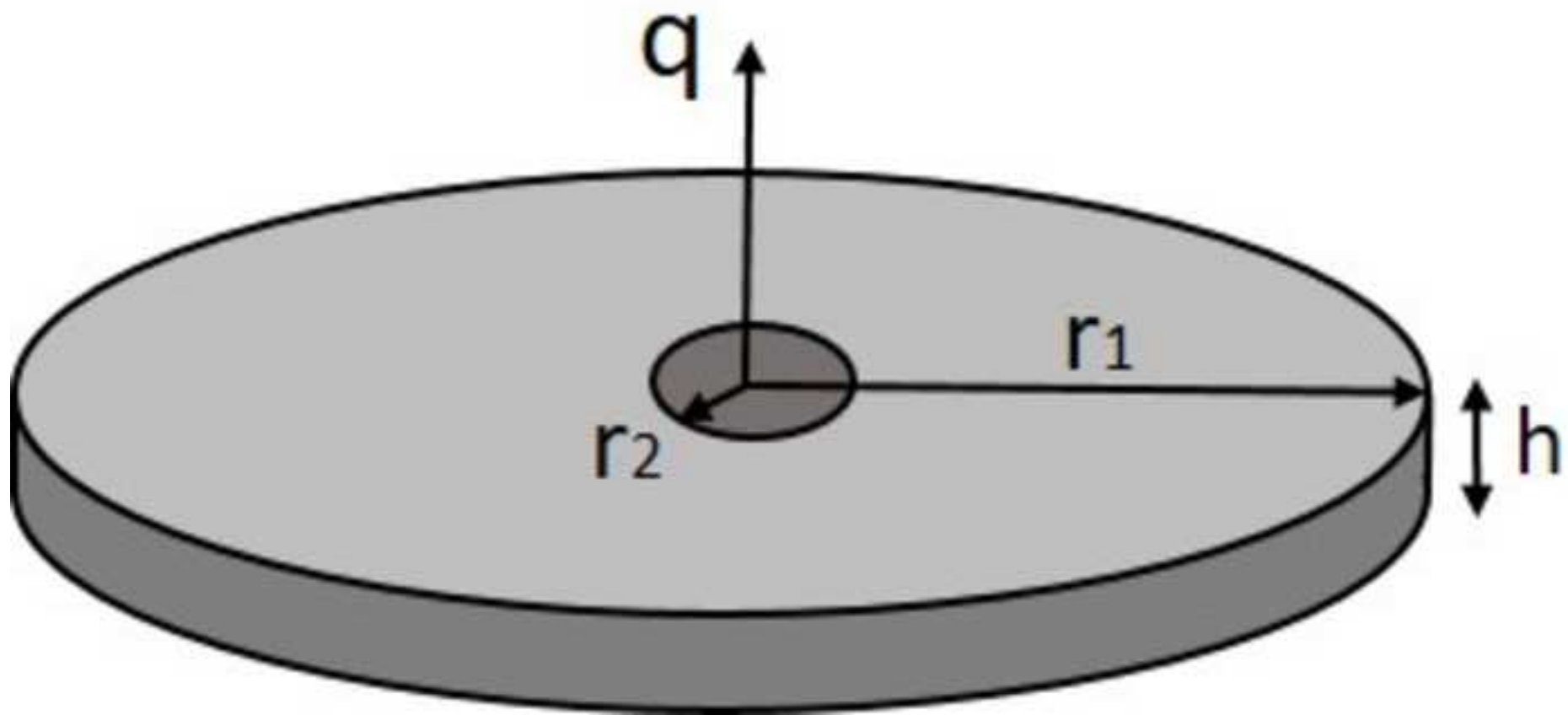


\* According to the standard API, RP 40, 7.6

DRX: X-Ray diffraction, SEM: Scanning Electron Microscope, CT: Computerized Tomography X (longitudinal), Y (axial), F (frontal)

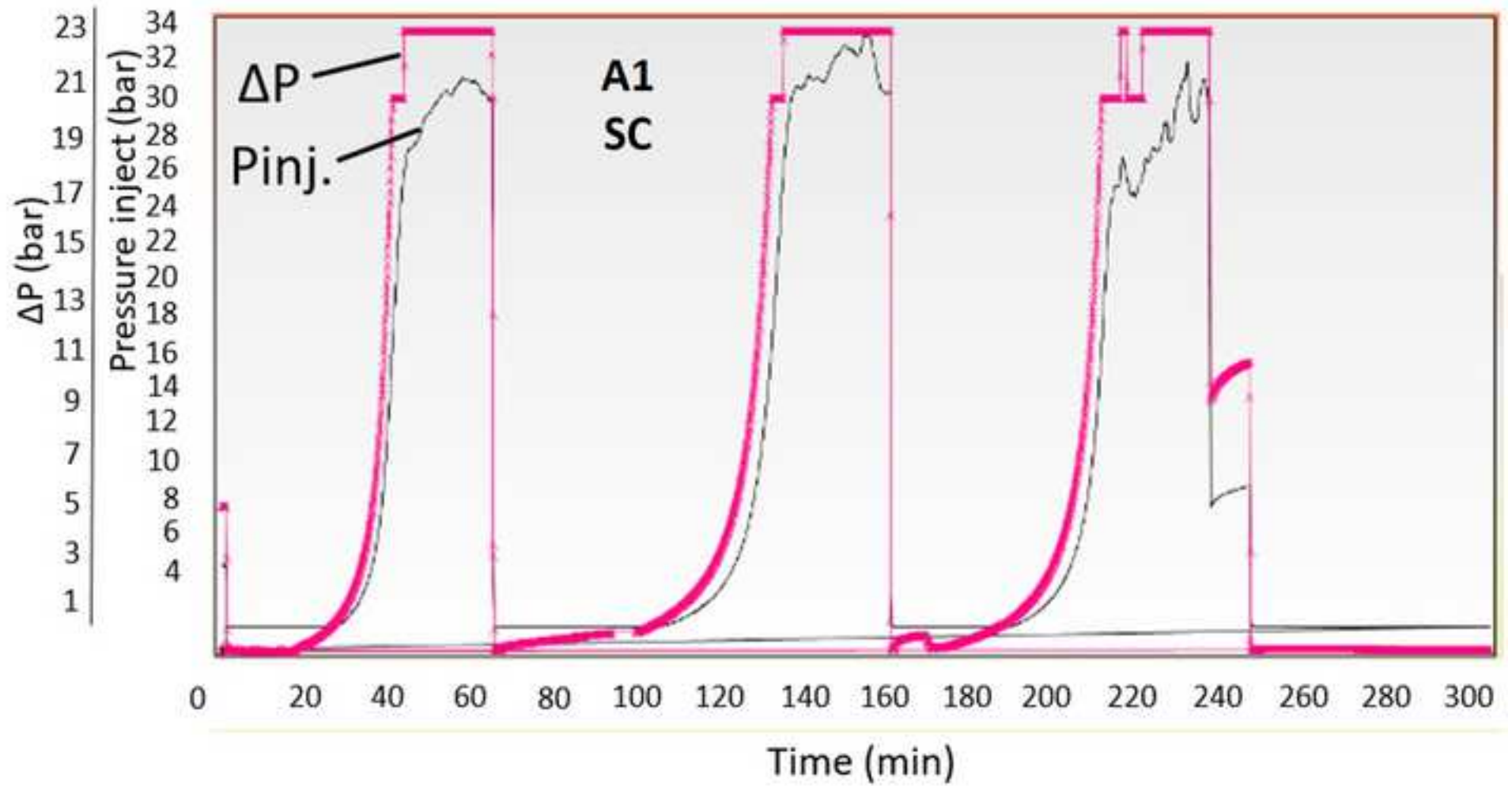
ATAP: Experimental facility, P: Pressure, T: Temperature, Pre) Pre-injection, Post) Post-injection.

Figure  
[Click here to download high resolution image](#)



Figure

[Click here to download high resolution image](#)



Figure

[Click here to download high resolution image](#)

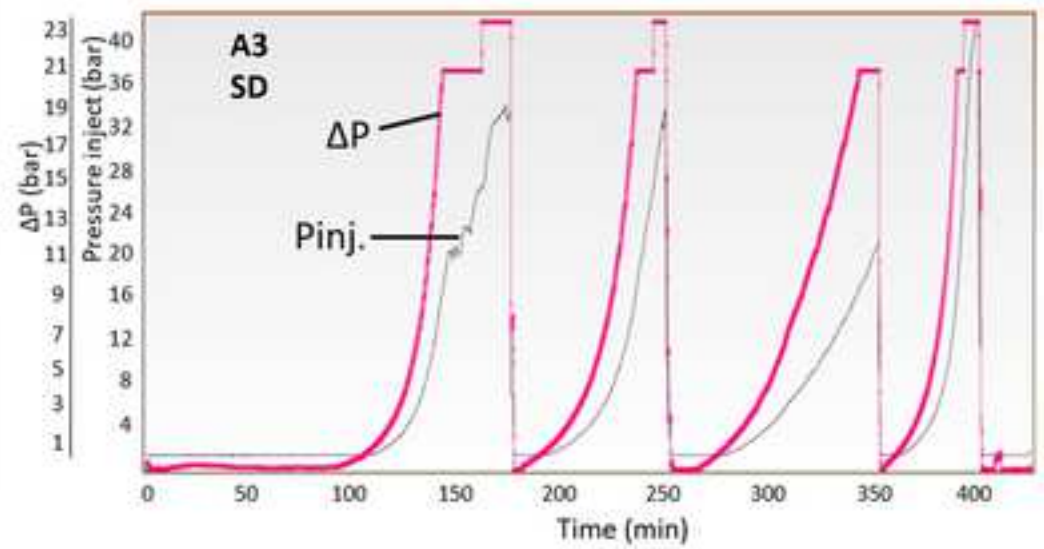
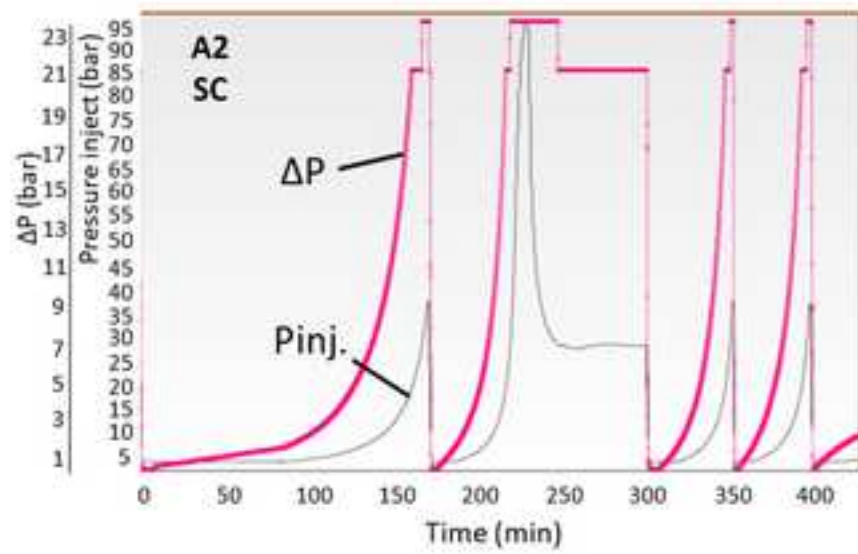


Figure  
[Click here to download high resolution image](#)

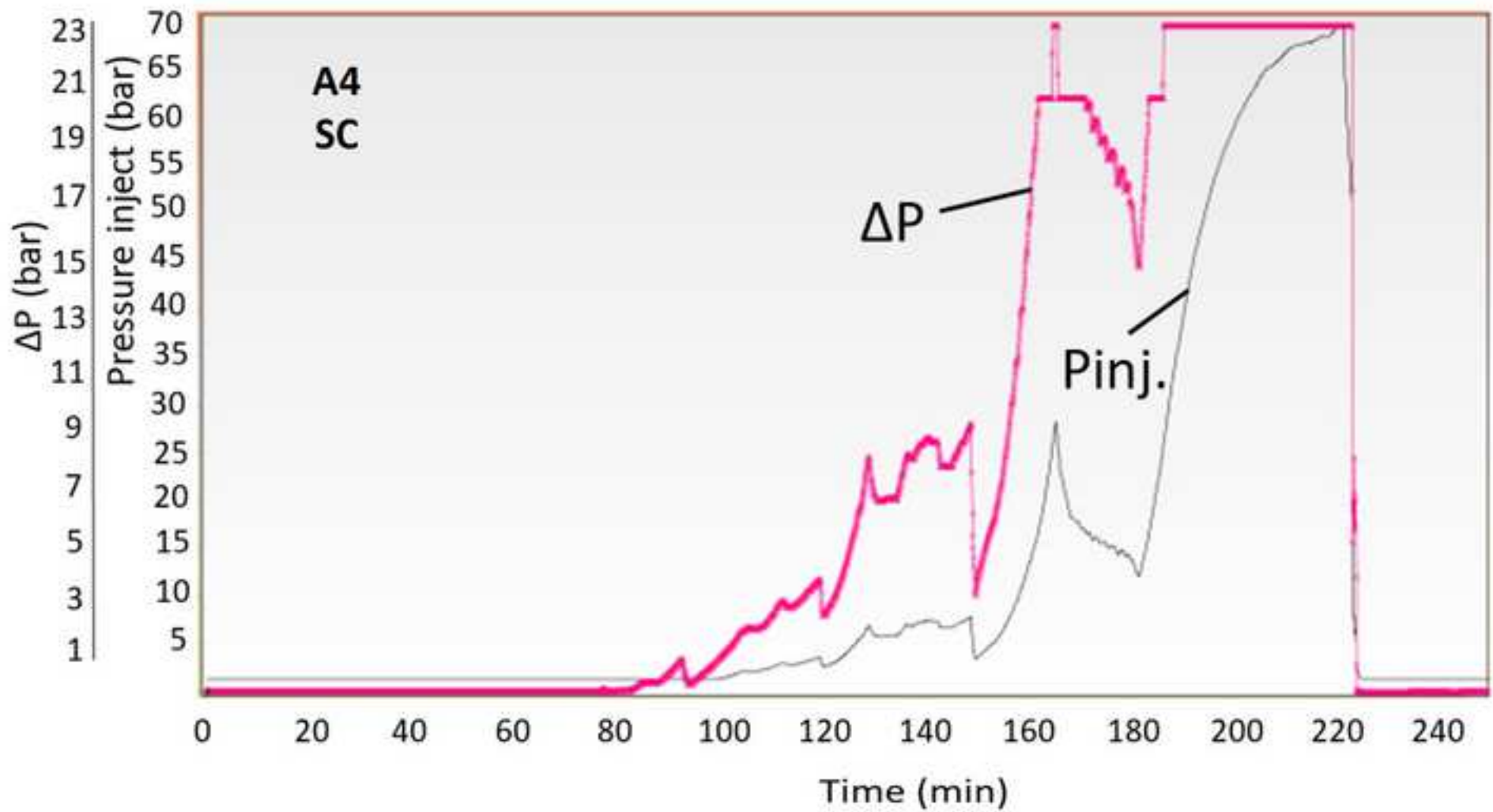


Figure  
[Click here to download high resolution image](#)

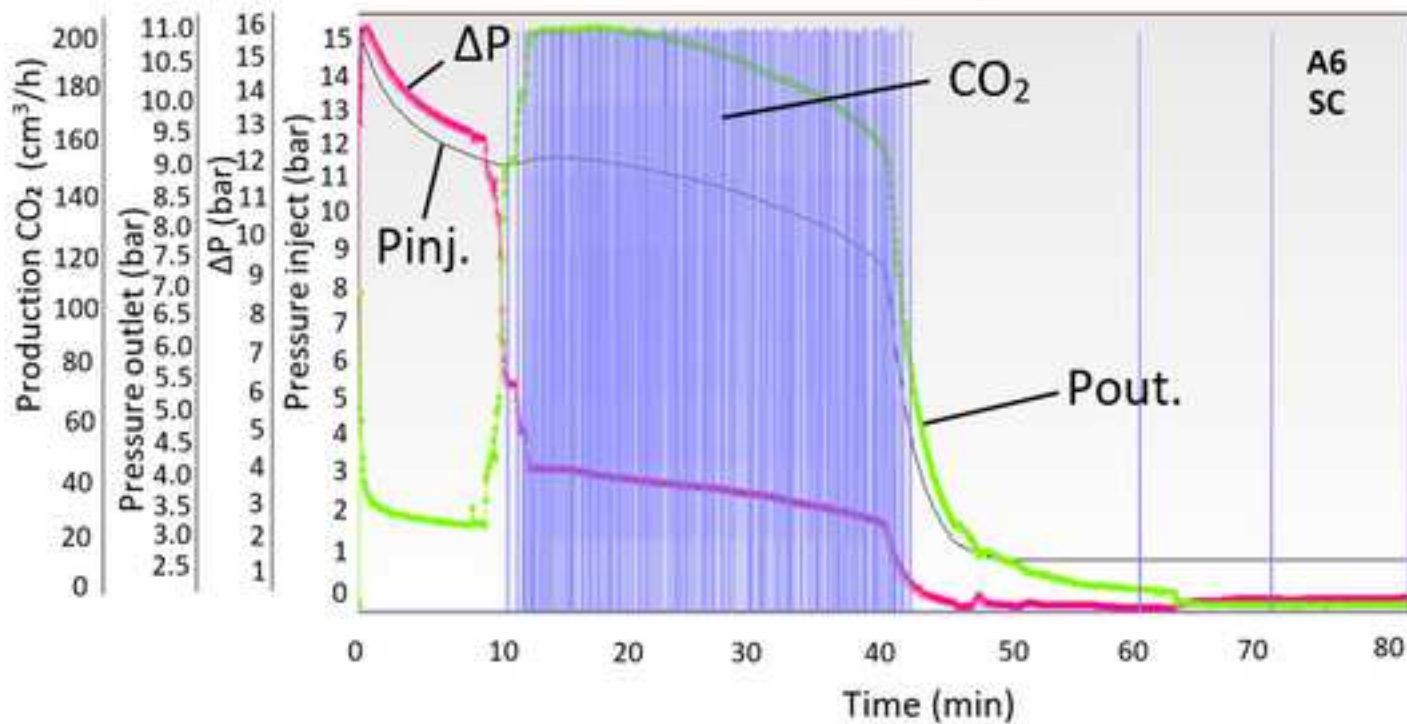
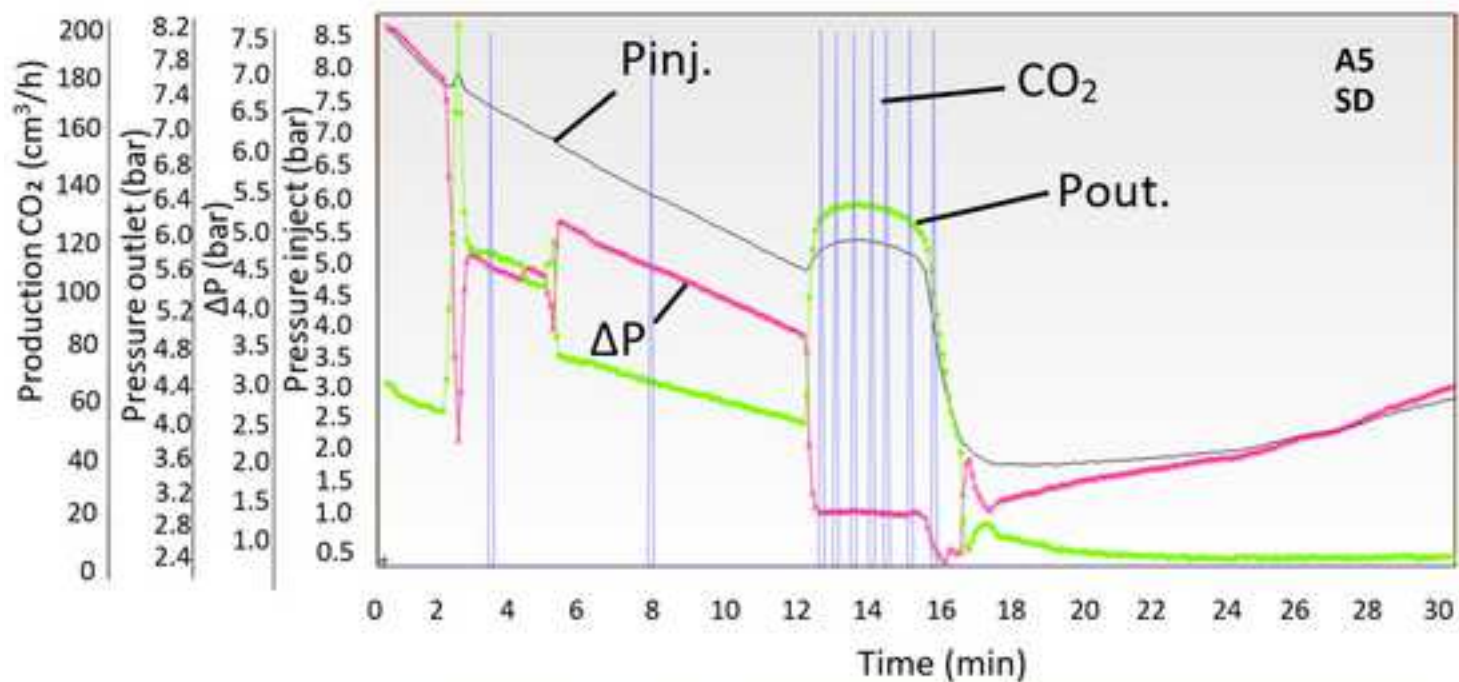
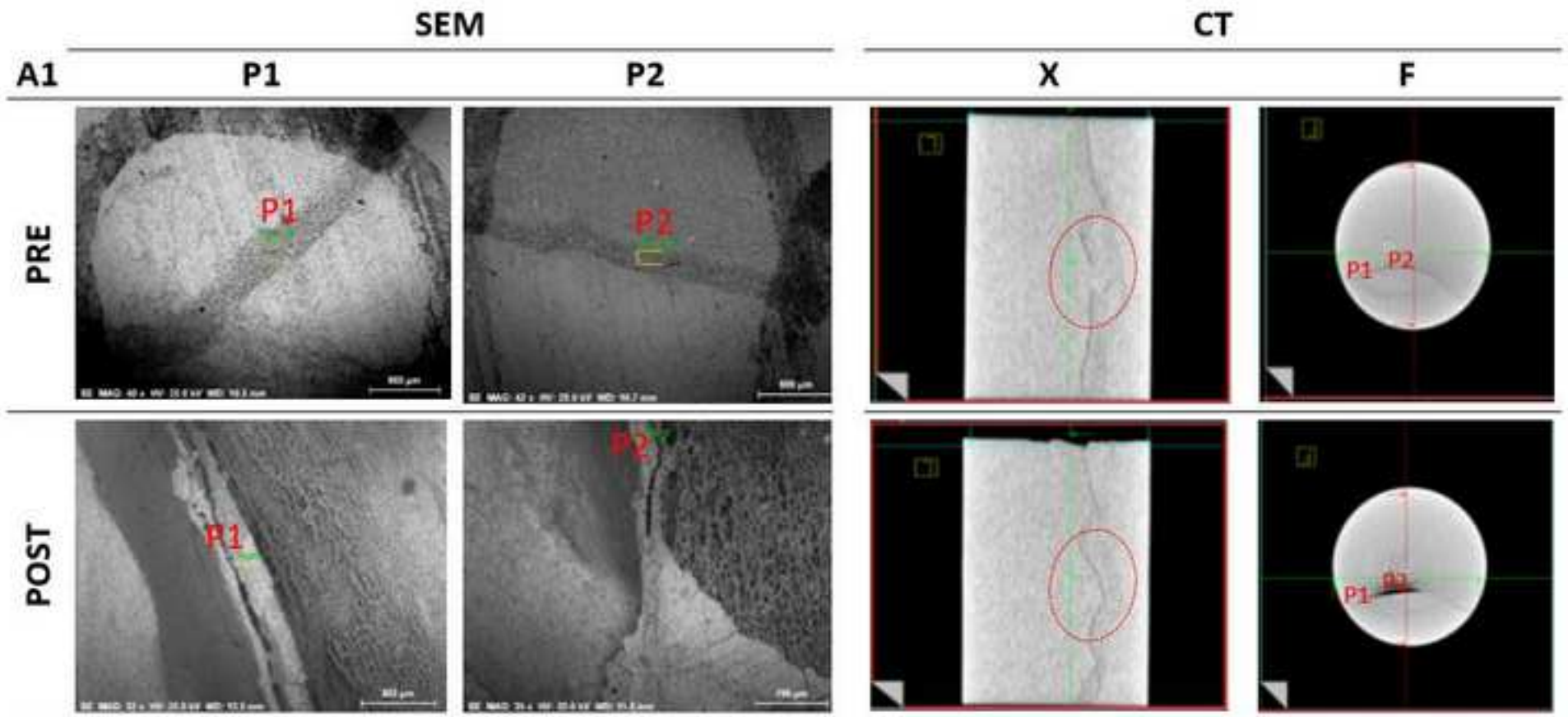
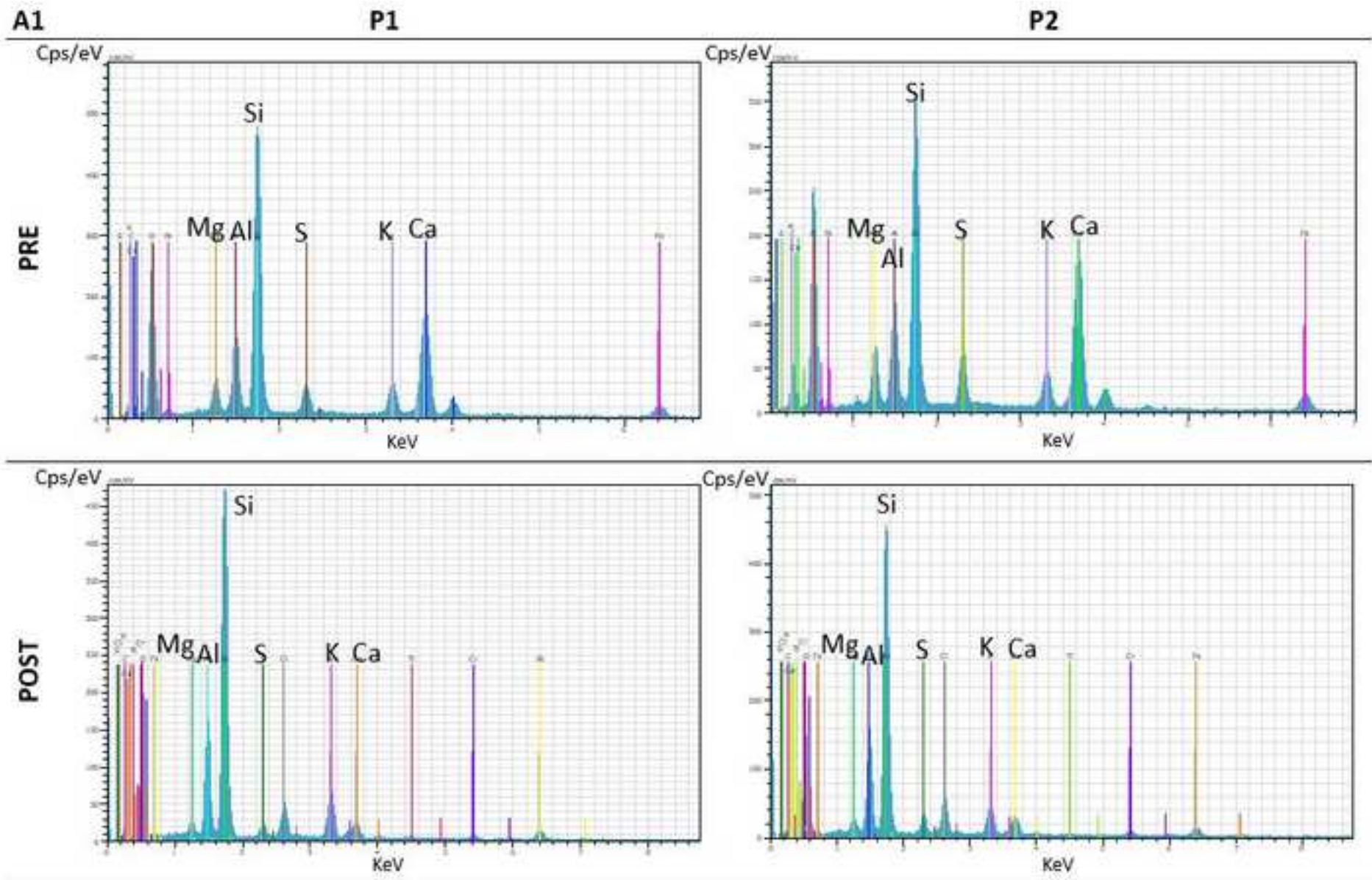


Figure  
[Click here to download high resolution image](#)



Figure

[Click here to download high resolution image](#)



Figure

[Click here to download high resolution image](#)

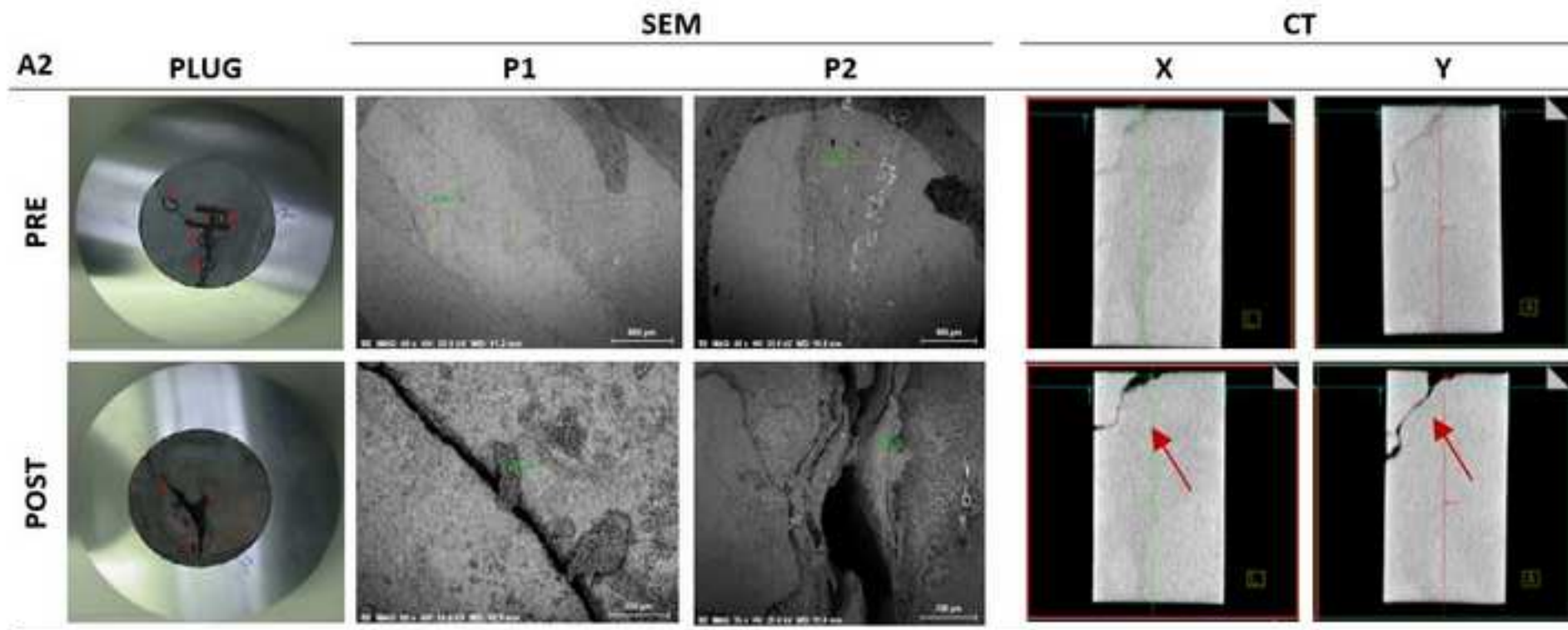
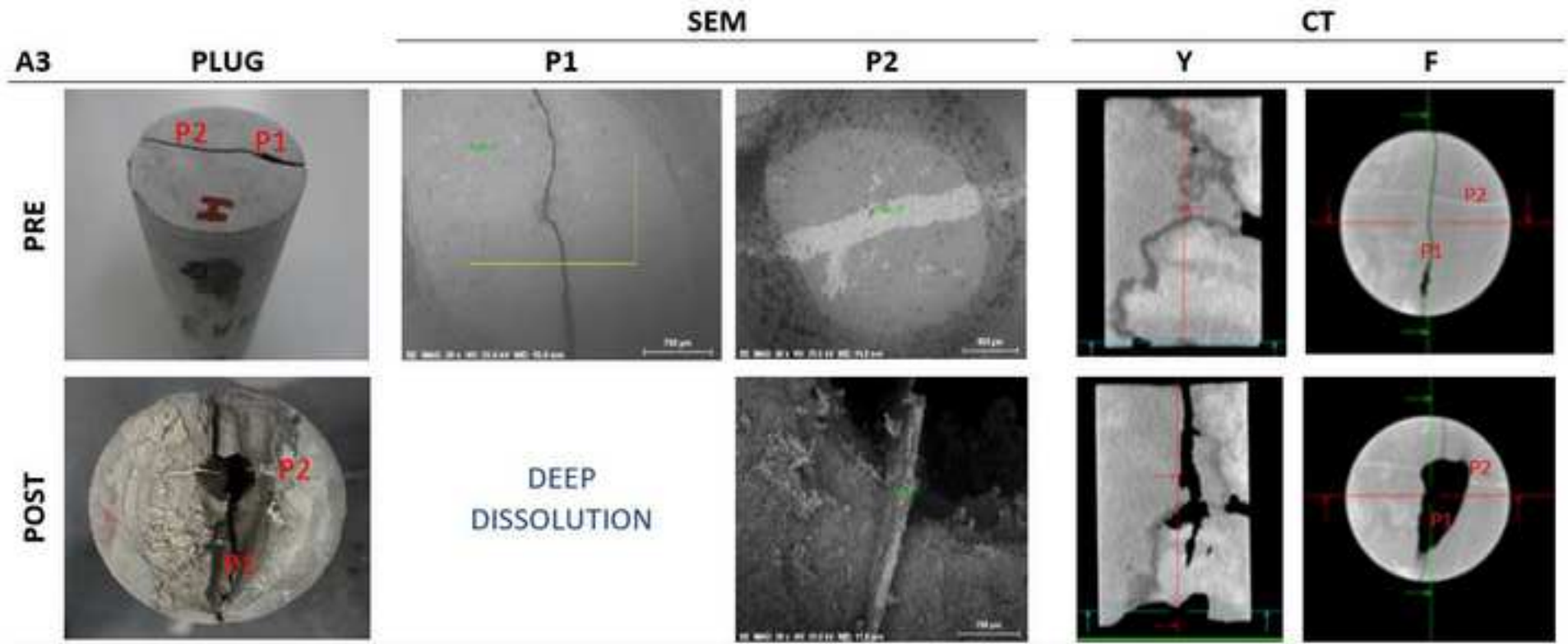
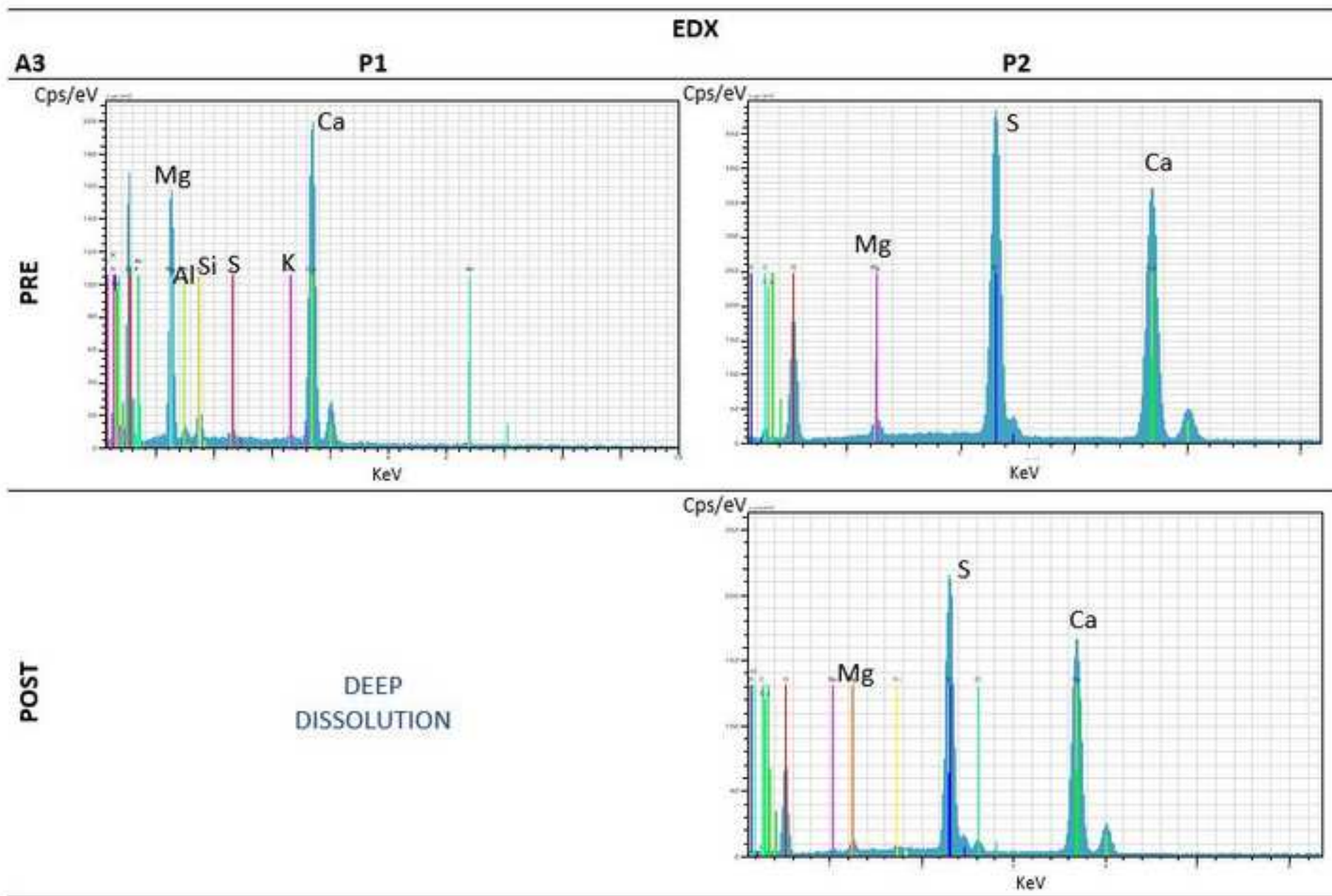


Figure  
[Click here to download high resolution image](#)



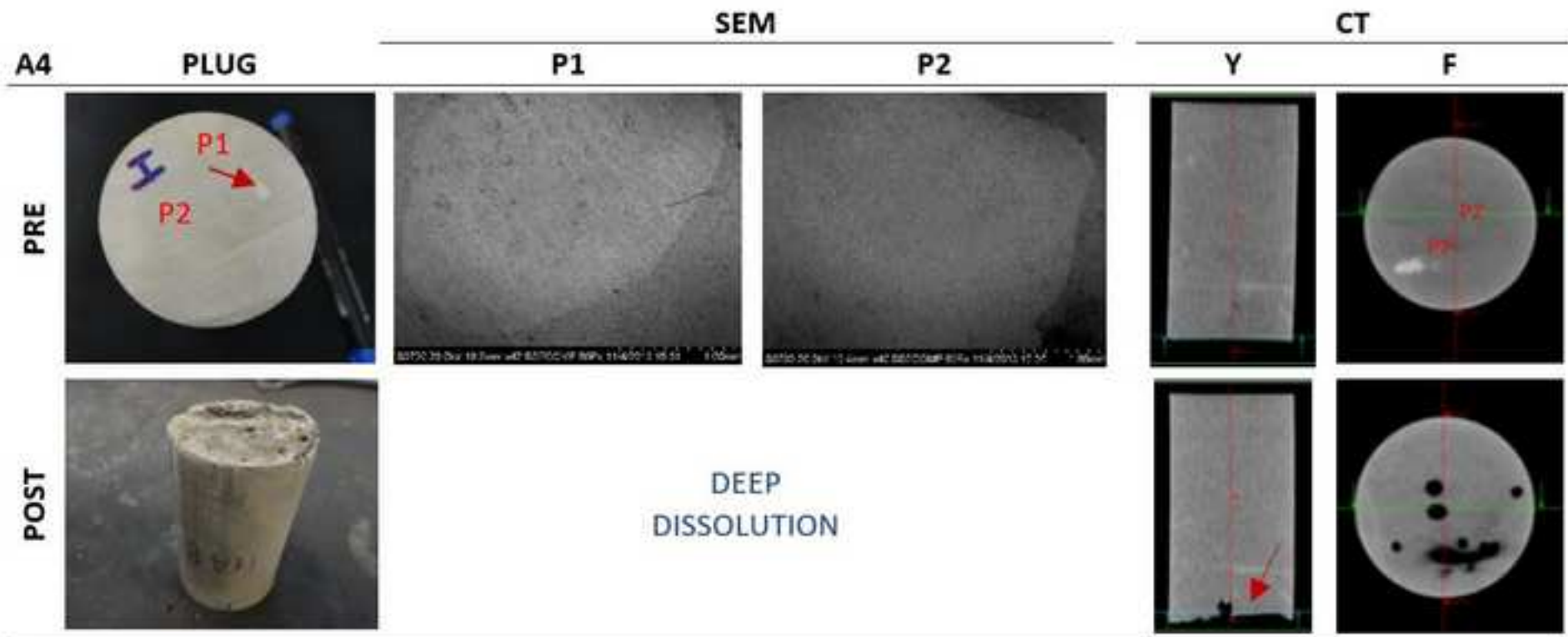
Figure

[Click here to download high resolution image](#)



Figure

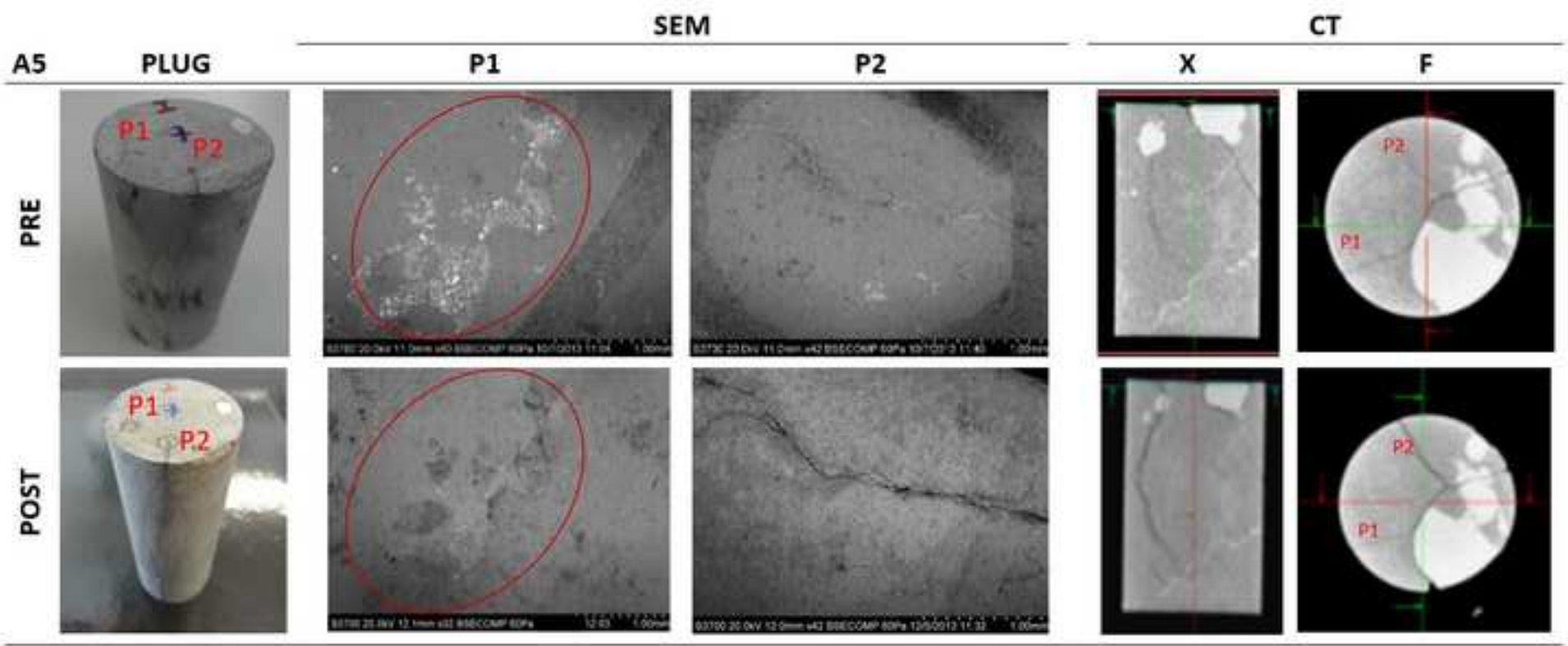
[Click here to download high resolution image](#)





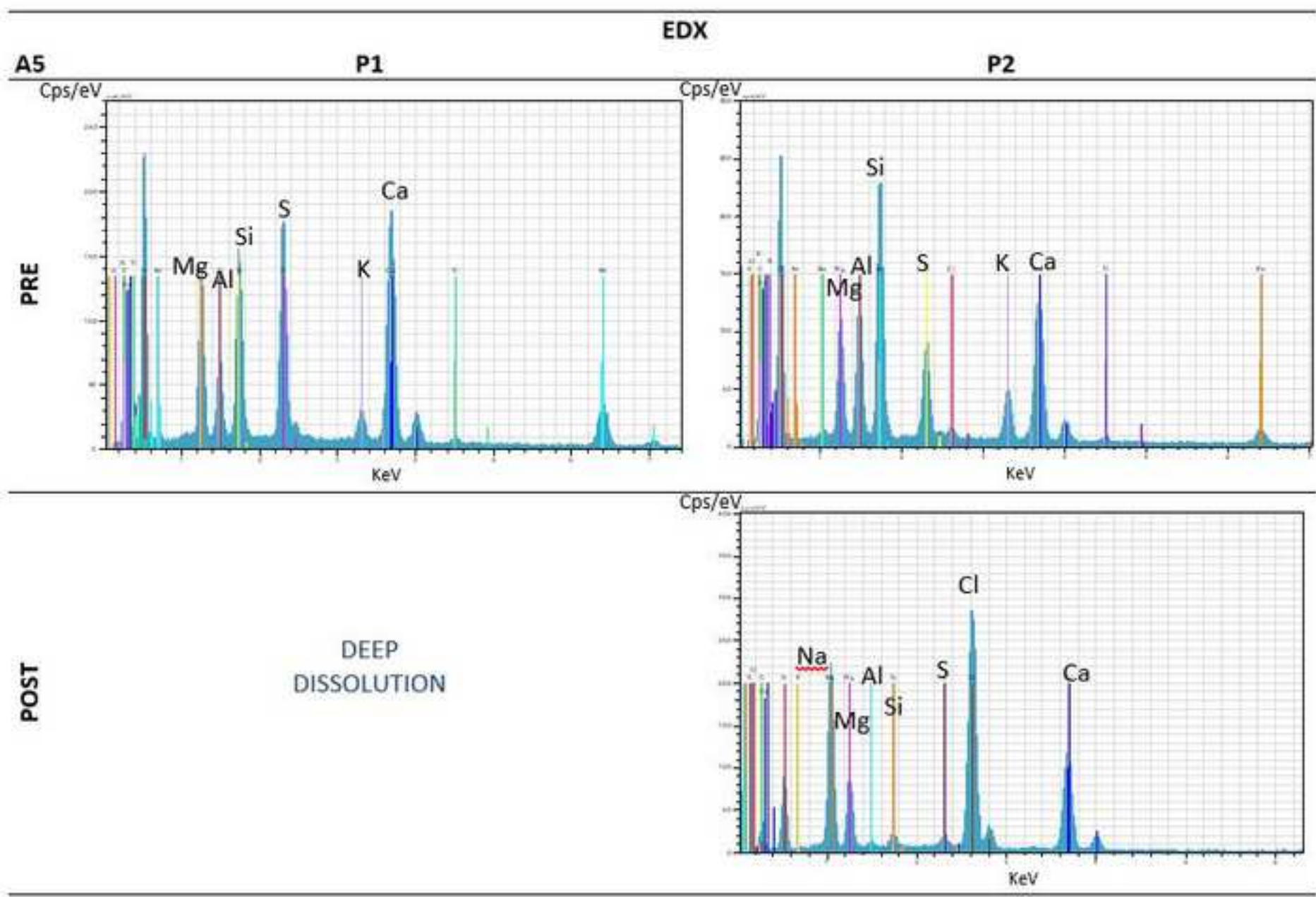
Figure

[Click here to download high resolution image](#)



Figure

[Click here to download high resolution image](#)



Figure

[Click here to download high resolution image](#)

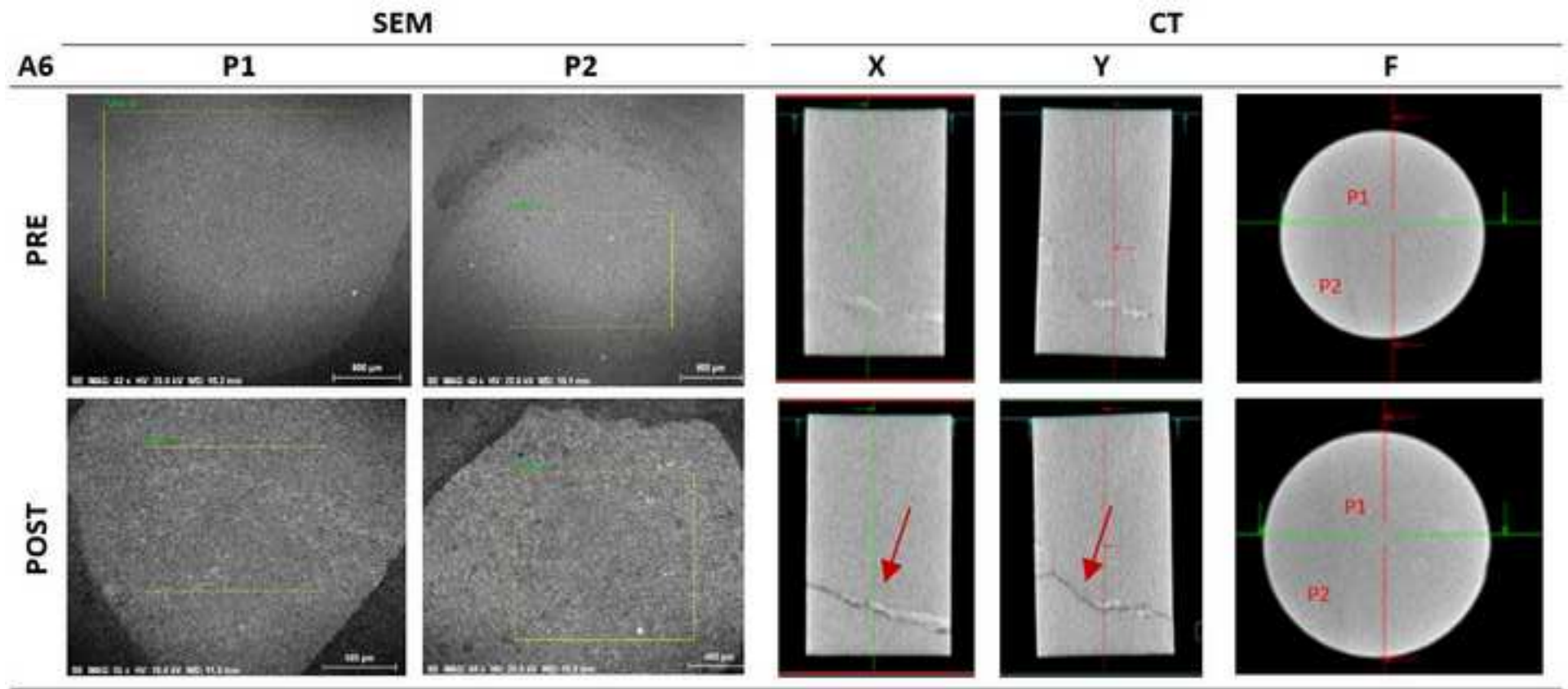
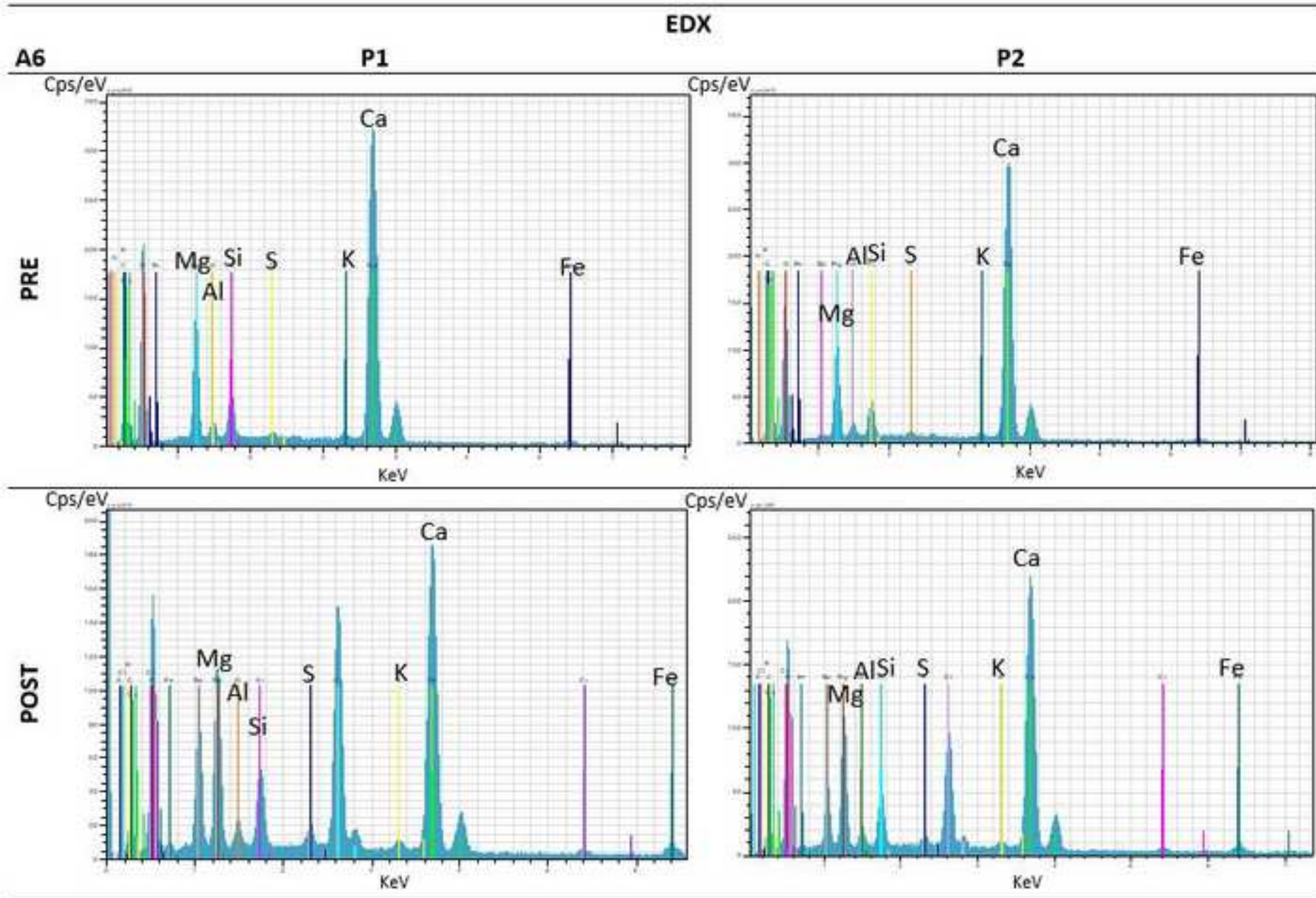


Figure  
[Click here to download high resolution image](#)



Sample		Depth (m)	Weight (g)	Length (mm)	Diameter (mm)	Volume			Grain Density (g/cm <sup>3</sup> )	Porosity (%)
ID	F <sub>d</sub>					Total cm <sup>3</sup>	Solid (cm <sup>3</sup> )	Pore(cm <sup>3</sup> )		
A1	SC	1448.3	204.42	67.41	37.90	76.03	75.86	0.17	2.69	0.22
A2	SC	1449.7	218.31	71.87	37.84	80.82	80.36	0.45	2.71	0.56
A3	SD	1518.5	217.61	72.24	37.86	81.31	76.61	4.69	2.84	5.77
A4	SC	1442.1	186.38	72.89	37.96	82.50	65.84	16.65	2.83	20.18
A5	SD	1525.7	230.39	74.06	37.82	83.20	81.28	1.91	2.83	2.30
A6	SC	1443.8	213.83	72.11	38.02	81.85	76.88	4.96	2.78	6.06

ID: sample identification; F<sub>d</sub>: geological formation Sopeña Calizo/Dolomítico (SC/SD)

Sample		Calcite	Dolomite	Quartz	Anhydrite
ID	F <sub>d</sub>	CaCO <sub>3</sub> (%)	CaMg (CO <sub>3</sub> ) <sub>2</sub> (%)	SiO <sub>2</sub> (%)	CaSO <sub>4</sub> (%)
A1	SC	91.6	7.6	0.7	-
A2	SC	55.5	4.1	3.5	-
A3	SD	-	95.1	0.1	4.8
A4	SC	-	99.1	0.9	-
A5	SD	-	90.5	0.2	9.3
A6	SC	19.9	79.6	0.5	-

*ID: sample identification; F<sub>d</sub>: geological formation Sopeña Calizo/Dolomítico (SC/SD)*

Sample		$W_s$ (g)		$W_s$ + dry filter (g)		Calcite %	Carbonate %
ID	$F_d$	20 °C	80 °C	20 °C	80 °C	20 °C	80 °C
A1	SC	1.022	1.016	0.149	0.148	93.83	93.89
A2	SC	1.040	1.087	0.171	0.168	91.82	92.08
A3	SD	1.057	1.100	0.101	0.097	98.48	98.90
A4	SC	1.009	1.004	0.126	0.125	86.85	95.80
A5	SD	1.010	1.069	0.112	0.111	97.33	97.47
A6	SC	1.094	1.090	0.154	0.153	90.42	91.75

*According to the standard API, RP 40, 7.6*

*ID: sample identification;  $F_d$ : geological formation Sopeña Calizo/Dolomítico (SC/SD);  $W_s$ : sample weight*

Sample	Injection mixture
A1 (SC)	10 % HCl
A2 (SC) & A3 (SD)	15 % HCl
A4 (SC)	10 % HCl & 10 % Acetic ( $\text{CH}_3\text{COOH}$ )
A5 (SD) & A6 (SC)	50 % $\text{scCO}_2$ & 50 % brine

**Declaration of interests**

The authors declare that they have no known competing financial interests or personal relationships that could have appeared to influence the work reported in this paper.

The authors declare the following financial interests/personal relationships which may be considered as potential competing interests: